Journal of Nuclear Medicine, published on January 20, 2022 as doi:10.2967/jnumed.121.263221

Molecular imaging of Neuroendocrine Prostate Cancer by targeting Delta-like Ligand 3

Joshua A. Korsen[1,2], Teja M. Kalidindi[1], Samantha Khitrov[1], Zachary V. Samuels[1], Goutam Chakraborty[3,4], Julia A. Gutierrez[1], John T. Poirier[5], Charles M. Rudin[2,3], Yu Chen[3,6], Michael J. Morris[3], Naga Vara Kishore Pillarsetty[1*], and Jason S. Lewis[1,2*]

[1]Department of Radiology, Memorial Sloan Kettering Cancer Center; New York, NY, USA.
[2]Department of Pharmacology, Weill Cornell Medicine; New York, NY, USA.
[3]Department of Medicine, Memorial Sloan Kettering Cancer Center; New York, NY USA.
[4]Department of Urology, Icahn School of Medicine at Mount Sinai, New York, NY USA.
[5]Perlmutter Cancer Center, New York University Langone Health; New York, NY, USA.
[6]Human Oncology and Pathogenesis Program, Memorial Sloan Kettering Cancer Center; New York, NY, USA.

Running Title: DLL3 PET imaging in NEPC

Keywords: Neuroendocrine prostate cancer, ImmunoPET, Molecular imaging, DLL3

***Co-Corresponding authors:**

*Naga Vara Kishore Pillarsetty, Department of Radiology, Memorial Sloan Kettering Cancer Center, 1275 York Avenue, 10065, USA; Email: pillarsn@mskcc.org; Phone: (646)888-2221

*Jason S. Lewis, Department of Radiology, Memorial Sloan Kettering Cancer Center, 1275 York Avenue, NY, 10065; Email: lewisj2@mskcc.org Phone: (646)888-3038

First Author (graduate student):

Joshua Aaron Korsen, Department of Radiology, Memorial Sloan Kettering Cancer Center, 1275 York Avenue, NY, 10065, USA; Email: korsenj@mskcc.org Phone: (516)567-1217

Word Count: 5243 words

Disclosure: Authors declare that they have no competing interests.

Financial Support: The study was supported in part by NIH T32 GM073546 (JAK). The Radiochemistry and Molecular Imaging Probes Core Facility, the Small Animal Imaging Facility, and the Molecular Cytology Core Facility were supported in part by NIH P30 CA08748. This study was also supported in part by NIH R35 CA232130-01A1 (JSL), R35 CA263816 (CMR), and Geoffrey Beene Cancer Research Center (JSL, KP, CMR, YC). GC is supported by a Prostate Cancer Foundation Young Investigator Award.

Abstract: Treatment-induced neuroendocrine prostate cancer (NEPC) is a lethal subtype of castration-resistant prostate cancer (CRPC). Using the zirconium-89 (^{89}Zr)-labeled DLL3 targeting antibody SC16 (^{89}Zr-DFO-SC16), we have developed a positron emission tomography (PET) agent to non-invasively identify the presence of DLL3-positive NEPC lesions. **Methods:** qPCR and immunohistochemistry were used to compare relative levels of androgen receptor (AR)-regulated markers and NEPC marker DLL3 in a panel of prostate cancer cell lines. PET imaging with ^{89}Zr-DFO-SC16, ^{68}Ga-PSMA-11, and ^{68}Ga-DOTA-TATE was performed in H660 NEPC xenografted male nude mice. ^{89}Zr-DFO-SC16 uptake was corroborated by biodistribution studies. **Results:** *In vitro* studies demonstrate H660 are positive for DLL3 and negative for AR, prostate-specific antigen (PSA), and prostate-specific membrane antigen (PSMA) both at the transcriptional and translational levels. PET imaging and biodistribution studies confirm ^{89}Zr-DFO-SC16 uptake is restricted to H660 tumor xenografts with background uptake in non-NEPC lesions (both AR-dependent and AR-independent). Conversely, H660 xenografts cannot be detected with imaging agents targeting PSMA (^{68}Ga-PSMA-11) or somatostatin receptor subtype 2 (SSTR2) (^{68}Ga-DOTA-TATE). **Conclusion:** These studies demonstrate H660 NEPC cells selectively express DLL3 on their cell surface and can be non-invasively identified with ^{89}Zr-DFO-SC16.

INTRODUCTION

Androgen receptor (AR) signaling is a critical driver of prostate cancer (PC). Androgen deprivation therapy (ADT) is used in the setting of high-risk, recurrent, or metastatic PC. Although ADT can initially be highly effective, resistance develops in most patients leading to metastatic castration-resistant prostate cancer (mCRPC) and ultimately death. Treatment resistance to ADT in mCRPC arises from multiple mechanisms including (1) AR amplification, (2) AR bypass, and (3) complete AR independence (*1*). The introduction of more potent AR signaling inhibitors (ARSIs, e.g., abiraterone, enzalutamide), has led to an increasing incidence of lesions in mCRPC patients that may display AR loss or adapt to low androgen levels through activation of alternative pathways (*2*). AR-independent tumors can be aggressive and can demonstrate markedly elevated proliferation, enhanced capacity for organ metastasis, and phenotypic heterogeneity with variable admixture of adenocarcinoma and small cell neuroendocrine phenotypes (*2*). Treatment-induced neuroendocrine prostate cancer (NEPC) has been shown to arise from treatment-induced lineage plasticity and lead to a highly aggressive and lethal subtype of PC (*3*). This reprogramming is linked to the reactivation of developmental transcriptional programs and the transcription factor SOX2, which promotes phenotypic plasticity and acquisition of a stem-like phenotype (*4*)**.** NEPC displays genetic similarities to small cell lung cancer (SCLC) including frequent loss of tumor suppressor genes *TP53* and *RB1* (*5*).

The lineage transcription factor achaete-scute complex homologue 1 (ASCL1) is overexpressed and promotes tumorigenesis in mouse models of SCLC (*6*). ASCL1 plays a key role in suppressing Notch signaling activity through markedly upregulated expression of the inhibitory Notch ligand delta-like ligand 3 (DLL3) (*7*). DLL3 expression in adult tissues is

substantially lower and restricted to intracellular compartments such as the Golgi; in contrast, in SCLC tumor cells it is aberrantly expressed on the cell surface (*7*). In PC, DLL3 has been shown to be similarly dysregulated in most NEPC samples (76.6%), with minimal to no expression in mCRPC (12.5%), localized PC (0.5%) and benign prostate (0%) (*8*). With no detectable expression of cell surface DLL3 in non-malignant cells and preferential expression in NEPC lesions, DLL3 may present itself as a target for a biomarker-based method of tumor detection.

SC16 is a humanized monoclonal antibody (mAb) that selectively binds to both human and murine DLL3 (*9*). Our previous work with SC16 has demonstrated the successful synthesis of zirconium-89 (^{89}Zr)-radiolabeled SC16 and its use as a positron emission tomography (PET) radiopharmaceutical for non-invasive detection of DLL3 expression in SCLC models (*10*). PET is a powerful diagnostic tool that can non-invasively visualize and molecularly characterize lesions and aid in optimizing therapy. It has proven to be a successful platform in PC detection and management of AR-dependent lesions. However, the 2018 NCI Workshop on Lineage Plasticity and Androgen Receptor-Independent Prostate Cancer identified a "lack of imaging capabilities" as one of two major knowledge gaps in NEPC management (*11*). The PET probes thus far developed directly target AR (*12*) or prostate-specific membrane antigen (PSMA) (*13*) and may not detect NEPC lesions if they display AR loss or PSMA suppression (*14*) . Therefore, it is imperative to have a non-PSMA based imaging agent for NEPC detection. To our knowledge, ^{89}Zr-radiolabeled SC16 is the only imaging agent currently in development that has potential to differentiate NEPC from prostate adenocarcinoma by an increase in signal above background. This is advantageous over current PET imaging agents that target AR-dependent PC, as reduced expression of these surface antigens is possible. This can increase susceptibility to high false positives or inconclusive findings when signal approaches the noise floor. Due to

the molecular similarities with SCLC and encouraging results from the preclinical studies in SCLC models, we evaluated the performance of our ^{89}Zr-radiolabeled SC16 PET imaging agent in the detection of DLL3-expressing NEPC tumors in preclinical mouse models.

MATERIALS AND METHODS

Please refer to the Supplementary Information for information related to cell lines, quantitative real-time PCR, antibody functionalization and radiolabeling (*15*), *in vitro* binding assays (*16*), immunohistochemistry, and generation of subcutaneous xenograft models.

Animals and Tumor Models

All animal experiments performed in this study were approved by the Institutional Animal Care and Use Committee and Research Animal Resource Center at Memorial Sloan Kettering Cancer Center.

Biodistribution Studies

Biodistribution studies were performed by sacrificing mice at chosen time points to evaluate uptake of the radiotracers in mice bearing subcutaneous H660 or DU145 tumors. To evaluate non-specific uptake in the DLL3-positive tumor, mice bearing subcutaneous xenografts of H660 were injected with isotype-matched IgG ^{89}Zr-DFO-IgG. See supplemental information for further details.

PET/CT Imaging

PET imaging of subcutaneous PC cell line xenograft mouse models was performed on an Inveon microPET/CT instrument (Siemens). See supplemental information for further details.

Statistical Analyses

All data presented are expressed as mean ± SEM. Data for the *in vitro* cell binding assay were analyzed by unpaired, two-tailed *t* test using GraphPad Prism 8 software with a threshold for statistical significance set as $p < 0.05$. To evaluate the blocking study in the subcutaneous xenograft, a 2-way ANOVA test using GraphPad Prism 8 software was performed with a threshold for statistical significance set at $p < 0.05$. A correction for multiple comparisons was performed using the Holm-Sidak method to determine statistical significance ($\alpha = 0.05$).

RESULTS

Evaluation of DLL3 Expression in Neuroendocrine Prostate Cancer

We evaluated mRNA and protein expression of AR and SOX2 transcription factors and their downstream targets that have been shown to differentiate adenocarcinoma or neuroendocrine phenotype respectively, in established PC cell lines using qRT-PCR and immunohistochemistry. For prostate adenocarcinoma genes, we evaluated *FOLH1* (gene encoding for PSMA) and *KLK3* (gene encoding for prostate-specific antigen (PSA)); for neuroendocrine regulated genes we examined *ASCL1* and *DLL3*. The panel of PC cell lines included LNCaP (hormone-sensitive prostate adenocarcinoma, AR+/NE-), DU145 (androgen-independent prostate carcinoma, AR-/NE-), PC3 (androgen-independent prostate carcinoma, AR-/NE-) and H660 (NEPC, AR-/NE+). H660 expressed the highest of *SOX2,* which encodes a transcription factor that promotes lineage

plasticity, facilitates histological transformation, and has been associated with resistance to AR-targeted therapies (*5,17*). PC3, LNCaP, and DU145 all demonstrated significantly lower levels of *DLL3*. H660 cells showed *ASCL1* expression, encoding a key transcription regulator of Notch signaling proteins, including DLL3 (Fig. 1A). At protein-level, using immunohistochemistry, we could detect DLL3 expression only in the H660 line but not in the other PC lines (Fig. 1B). Verification of the NEPC lineage of H660 was confirmed by the presence of the clinically validated NE marker synaptophysin (SYP), which was absent in all LNCaP, PC3, and DU145 cell lines (Fig. 1B). When transcript levels of *AR*, *KLK3*, and *FOLH1* levels were evaluated, only LNCaP cells showed expression, while H660, PC3, and DU145 had minimal detectable transcripts (Fig. S1A). Immunohistochemistry provided similar results at the translational level, demonstrating intense staining of AR and PSMA in LNCaP cells with no detectable expression seen in H660, PC3, and DU145 (Fig. S1B).

We then analyzed the PC transcriptomic atlas dataset (*18*), an extensive transcriptome databank comprised of 1,321 clinical specimens from 38 PC cohorts. We observed higher expression of *DLL3* in mCRPC compared to primary PC ($p < 0.001$ mCRPC VS Primary; Fig. S2A). Moreover, in the Ross Adams et al. cohort (*19*) (259 men with PC in Cambridge discovery cohort and Stockholm validation cohort), we observed high *DLL3* expression was associated with shorter biochemical recurrence-free survival (Fig. S2B). Together these data indicated that *DLL3* mRNA expression may be associated with poor prognosis of PC patients. This hypothesis will require further testing in a larger cohort to confirm the prognostic significance of *DLL3* mRNA expression in PC.

We next compared the expression levels of DLL3 in H660 and H82 tumor cells. H82 was derived from the pleural fluid of a patient with SCLC and H660 derived from the lymph node of

a NEPC patient. Both cell lines display neuroendocrine phenotype and aberrant DLL3 trafficking to the cell surface. Despite low expression of DLL3 on H82 cells, PET imaging successfully delineated H82 tumor in mouse models (*10*). Immunohistochemistry demonstrated even lower abundance of DLL3 expression in the H660 tumor cells compared to H82 tumor cells (Fig. S3). However, we still envisioned that DLL3-PET imaging would be feasible due to the absence of DLL3 expression on the cell surface of non-malignant cells.

^{89}Zr-DFO-SC16 Characterization and Its Detection of Cell Surface DLL3 Expression

The DLL3-targeting SC16 antibody was functionalized through the non-site-specific conjugation to the free lysine moieties available on the mAb with the siderophore-derived desferrioxamine (DFO) chelator (Fig. S4). MALDI-TOF MS analysis revealed the ratio of chelator to mAb was 0.44, which implies that, on average, half of the antibody molecules were functionalized with DFO covalently. (Fig. S5).

Radiolabeling the DFO-SC16 conjugate obtained ^{89}Zr-DFO-SC16 in high radiochemical yield (> 99%) (Fig. S6A) and high specific activity (370 Mbq/mg). The radioimmunoconjugate demonstrated ≥ 92% stability when incubated in human serum at 37 ºC for 5 days (Fig. S6B). The target-binding fraction (TBF) of the radioimmunoconjugate — the fraction of the antibody that retains its binding to its target after modification — was > 90% for ^{89}Zr-DFO-SC16 towards DLL3 (Fig. 2A). ^{89}Zr-DFO-SC16 binding to DLL3 could be blocked in the presence of a 5000-fold excess of unlabeled SC16. *In vitro* cell binding assays revealed ^{89}Zr-DFO-SC16 bound to DLL3 expressed on the cell surface of H660 cells with no binding observed in the DLL3-negative cell lines LNCaP, DU145, and PC3 (Fig. 2B). Binding of ^{89}Zr-DFO-SC16 to H660 cells could be blocked in the presence of a 1000-fold excess unlabeled SC16. Saturation binding assay

with H660 cells revealed K_d < 1 nM and B_{max} = 86.3 fm/10^6 cells for ^{89}Zr-DFO-SC16 (Fig. S6C). These studies demonstrate that the immunoreactivity of SC16 is retained after DFO conjugation and radiolabeling with zirconium-89.

PET imaging and Biodistribution of DLL3 Expression With ^{89}Zr-DFO-SC16 in Subcutaneous Xenograft Models

PET imaging with ^{89}Zr-DFO-SC16 was performed in male nude mice bearing H660 (DLL3+, AR-/NE+) or DU145 (DLL3-, AR-/NE-) subcutaneous xenografts. PET imaging with ^{89}Zr-DFO-SC16 showed clear delineation of H660 tumor xenografts 120 h post-administration of the radioimmunoconjugate (Fig. 3A). Increasing uptake in the H660-bearing mice could be observed in the tumors from time of injection (t = 0) to 120 h post-injection. As expected, due to lack of DLL3 expression, minimal uptake of ^{89}Zr-DFO-SC16 was observed in DU145-bearing mice with tumor uptake remaining constant over the 120 h imaging time course (Fig. 3B). Low and non-specific uptake was observed in H660 tumor xenografts 120 h post-injection of isotype-matched IgG (^{89}Zr-DFO-IgG) (Fig. S7A-C).

Biodistribution data at 24, 72, and 120 h after intravenous administration confirmed a progressive increase in H660 tumor uptake over time, reaching 17.50 ± 3.19 percentage injected dose per gram (%ID/g) at 120 h (Fig. 4A; Fig. S8). As expected, concurrent decrease in the blood pool activity was observed (24 h, 6.60 ± 0.90 %ID/g; 72 h, 3.16 ± 1.37 %ID/g; 120 h, 3.07 ± 0.45 %ID/g) as the tumor activity increased over time. Due to heterogenous uptake of the radioimmunoconjugate between the H660 tumors, two independent cohorts of 3 mice each were evaluated at 120 h. Linear regression analysis displayed a positive correlation between time post-intravenous administration and %ID/g in H660 tumors across both independent cohorts, with

tumor uptake increasing over time (p = 0.00971; Fig. S9). Uptake of the radioimmunoconjugate could be blocked by the co-injection of a 50-fold excess of unlabeled SC16 antibody, confirming the specificity of the radioimmunoconjugate for the H660 tumor (Fig. 4A; Fig. S10). At 120 h post-injection, high tumor-to-background contrast ratios were observed (Fig. 4B), with a tumor-to-muscle ratio = 33.91 ± 5.73. In contrast, ^{89}Zr-DFO-SC16 uptake in the DU145 (DLL3-) tumors was low and non-specific at 5.47 ± 0.25 %ID/g 120 h post-intravenous administration, consistent with an *in vivo* enhanced permeability and retention effect (Fig. 4C; Fig. S11). Comparing tumor uptake at each time point in the H660 and DU145 tumors demonstrates ^{89}Zr-DFO-SC16's specificity and selectivity for DLL3 (Fig. S12A). H660 tumor mean uptake increased over time and was statistically significant when compared to DU145 tumor mean uptake at 72 and 120 h post injection. Tumor-to-muscle ratios also increased over time in the H660 tumors and were statistically significant at 72 and 120 h post injection when compared to DU145 tumors, in which this ratio remained relatively constant at all time points (Fig. S12B). Considering potential clinical implications, taken together these data suggest patients could be effectively imaged in a wide time window (72 – 120 h). Immunohistochemistry on resected H660 subcutaneous xenografts confirmed retained expression of DLL3 and SYP, which were absent in resected DU145 subcutaneous xenografts (Fig. 4D; See Fig. S13 for SYP immunohistochemistry and corresponding H&E).

NEPC is Only Detectable by DLL3 Imaging, but Not by PSMA or Somatostatin Imaging

To demonstrate the dichotomy between AR+ prostate adenocarcinoma and AR- NEPC, male nude mice were subcutaneously xenografted with PSMA+/DLL3- LNCaP tumors and PSMA-/DLL3+ H660 tumors on opposite flanks and imaged by DLL3 and PSMA based PET. The dual-

tumor bearing mice were imaged 1 h post-administration of gallium-68 labeled PSMA-11 (^{68}Ga-PSMA-11), a PSMA-targeted PET agent. The radiotracer accumulated exclusively in the LNCaP tumor and could be successfully imaged with high contrast (Fig. 5). The NEPC model H660 does not express AR or PSMA and H660 tumors could not be detected through PSMA-based imaging. Two days later, the same cohort of mice were administered ^{89}Zr-DFO-SC16 and imaged 5 days post-administration. The radiotracer selectively bound to the H660 tumor but not LNCaP and finally allowed for site-specific identification of the NEPC lesion.

Somatostatin receptor (SSTR) imaging has been widely used as a method to detect the presence of gastroenteropancreatic neuroendocrine neoplasms including the FDA-approved agent ^{68}Ga-DOTA-TATE. ^{68}Ga-DOTA-TATE is a peptide-based PET imaging agent that demonstrates high affinity for the somatostatin receptor subtype 2 (SSTR2) and has been tested in NEPC patients with inconclusive results (*20*). As a comparator, we sought to image tumor-bearing mice by ^{68}Ga-DOTA-TATE. We first analyzed *SSTR2* mRNA expression in H660 and LNCaP cells. We could not detect significantly upregulated *SSTR2* expression in H660 cells relative to LNCaP cells (Fig. S14A). Shifting to *in vivo* analysis, we conducted an imaging study with ^{68}Ga-DOTA-TATE in H660-bearing male nude mice. No accumulation of the radiotracer was observed in the tumor 1 h post-administration, demonstrating inability to detect this NEPC tumor through somatostatin receptor imaging (Fig. S14B).

DISCUSSION

NEPC is a lethal disease and detecting the presence of NEPC lesions non-invasively remains challenging. One of the barriers to understanding the biology of mCRPC is the inaccessibility of the tissue and consequent under-sampling of disease heterogeneity. Biopsies, the gold standard in

terms of phenotypic characterization with immunostaining, and genotypic characterization with next-generation sequencing techniques describe only a single lesion rather than the full diversity of the disease. Furthermore, bone biopsies are difficult because tumors are frequently embedded deep within the densely sclerotic bone, a result of exuberant hydroxyapatite deposition from tumoral stimulation of osteoblasts. Circulating tumor cells (CTCs) and cell free DNA (ctDNA) can be used to characterize the biology of mCRPC, and can reflect post-treatment changes in tumor burden, but cannot localize the emergence of resistant disease on a lesional level. A non-invasive, whole-body method for detecting the emergence of NEPC will overcome these limitations of standard methods of tumor analysis, allow for identification and characterization of lesions in real-time, and facilitate earlier intervention to improve patient survival. Here, we confirm that the NEPC cell line H660 is devoid of the commonly targeted prostate biomarkers AR, PSMA, and PSA, but selectively expresses DLL3 on the cell surface. However, it must be stated that this is an idealized preclinical model, and a varied range of prostate biomarker expression may still be observed in patients with NEPC lesions. In our previous work, using the SCLC tumor model H82, we successfully showed that, though expression of DLL3 is less abundant than other commonly imaged tumor-associated antigens (e.g., Her2, EGFR, PSMA), the highly tumor-restricted cell surface expression of DLL3 on SCLC allows for successful PET imaging (*10*). Although the expression levels of DLL3 observed in the H660 NEPC tumor cells were lower than in the H82 SCLC tumor cells, PET imaging was still feasible due to the absence of detectable cell surface DLL3 in non-malignant cells. We demonstrate that ^{89}Zr-DFO-SC16 shows high specific uptake in H660 (DLL3+) tumors through biodistribution studies and PET imaging. PET imaging in a dual tumor model with H660 (DLL3+/PSMA-) and LNCaP (DLL3-/PSMA+) tumor cells demonstrates the inability to detect PSMA- NEPC lesions with other

commonly used imaging approaches. Neuroendocrine differentiation in prostate adenocarcinoma lesions due to selective treatment pressure can lead to the activation of different pathways, including the possibility of low AR and low AR-pathway signaling, which may result in the inability to detect such lesions with ^{68}Ga-PSMA-11 (*14*) or other AR-targeted tracers such as ^{18}F-FDHT (*12,21*). Therefore, using ^{68}Ga-PSMA-11 only, NEPC lesions may not be detected.

DLL3 imaging can provide patient stratification and suggests rationale for DLL3-targeted therapeutic approaches. Four DLL3-specific therapies have been tested clinically: (1) the antibody-drug conjugate rovalpituzumab tesirine (Rova-T or SC16LD6.5), (2) the bispecific T cell engager (BiTE) AMG757, (3) the chimeric antigen receptor (CAR) T cell AMG119, and (4) the trispecific T cell engager (TriTAC) HPN328. RovaT therapy demonstrated minimal responses in SCLC and other neuroendocrine carcinomas (9/69; 13%) (*22*), while AMG757 (NCT03319940), AMG119 (NCT03392064) and HPN328 (NCT04471727) are currently being tested in SCLC patients in first-in-human studies. One avenue yet to be explored could utilize a targeted radionuclide therapy with lutetium-177 (^{177}Lu) in patients with detected DLL3-positive PC lesions via ^{89}Zr-DFO-SC16 PET. Recent work by our lab has demonstrated the exceptional efficacy of ^{177}Lu-labeled-SC16 for the treatment of SCLC in preclinical models (*23*).

Lastly, we demonstrate the inability to target SSTRs in a subcutaneous NEPC model. Reports on the presence of somatostatin receptors in NEPC have been contradictory and inconclusive, with some studies suggesting that SSTR2 expression is upregulated (*24,25*), while others have shown low or absent expression (*26,27*). Here we show that H660 tumor cells do not express somatostatin receptors and therefore cannot be imaged *in vivo* through somatostatin-based receptor PET imaging.

Although DLL3 presents as a potential target for PET imaging in NEPC lesions, the biological consequences of PC treatments on pre-existing NEPC lesions are not understood. PC lesions in patients may have distinct adenocarcinoma, neuroendocrine, or mixed phenotypes. Therefore, even with detection of NEPC, patients may continue ADT. ADT influences the expression of PSA, PSMA, and block AR-targeting agents and therefore influences the outcomes of PET imaging studies with these agents (*28-30*). There is no clear understanding of the biological consequence of ADT on neuroendocrine cells or on the expression of DLL3. Likewise, it has been shown that the phosphatidylinositol 3-kinase (PI3K) pathway is activated in ADT-resistant mCRPC and influences the expression of neuroendocrine markers (*31*,*32*). Two PI3K inhibitors, everolimus (NCT00976755) and BKM-120 (NCT01385293) are currently in clinical trials for mCRPC. Further studies to evaluate the potential influence of PC treatments on NEPC lesions and DLL3 expression are warranted.

Overall, the selective expression of DLL3 in the tumor with no detectable expression in non-malignant cells and the high specificity of tumor uptake of ^{89}Zr-DFO-SC16 suggest the possibility of translating this imaging method into the clinic. With a clinical trial (NCT04199741) currently underway at Memorial Sloan Kettering Cancer Center — the first-in-human clinical trial of DLL3 PET imaging in patients with SCLC — our data encourages the use of DLL3 PET imaging in patients with NEPC lesions. Ultimately, DLL3-targeted PET imaging might confirm the presence of NEPC lesions through a non-invasive whole-body PET scan, aid patient selection, and may improve therapeutic outcomes in NEPC-directed clinical trials.

CONCLUSION

These findings suggest a non-invasive diagnostic PET agent that can be used as a tool to detect the presence of DLL3-positive NEPC lesions at single lesion resolution. We hope these findings will improve on the current approach of biopsy-based and genotypic characterization in identifying these patients.

Acknowledgments: The authors would like to acknowledge the Radiochemistry and Molecular Imaging Probes Core Facility, the Small Animal Imaging Facility, and the Molecular Cytology Core Facility. The graphical abstract and part of Figure 5 were made in Biorender.com.

Author contributions:

Conception and design: JAK, JTP, CMR, YC, KP, JSL

Development and methodology: JAK, JTP, CMR, YC, KP, JSL

Acquisition of data: JAK, TMK, SK, ZVS, GC, JG

Analysis and interpretation of data: JAK, TMK, GC, JTP, MJM, CMR, YC, NP, JSL

Writing, review and/or revision of the manuscript: All authors

Study supervision: JTP, CMR, YC, NP, JSL

KEY POINTS

Question: Can DLL3-targeted PET be used as a tool for the non-invasive diagnosis of NEPC?

Pertinent Findings: We demonstrated that DLL3 is exclusively expressed on the cell surface of H660 NEPC cell line and can be detected with DLL3-targeting tracer ^{89}Zr-DFO-SC16. *In vivo* PET imaging studies showed that ^{89}Zr-DFO-SC16 is selective for DLL3-expressing NEPC lesions and cannot be imaged with ^{68}Ga-PSMA-11 or ^{68}Ga-DOTA-TATE. The selective expression of DLL3 in the tumor and specific tumor uptake of ^{89}Zr-DFO-SC16 suggests potential translation of this imaging method to the clinic.

Implications for Patient Care: PET imaging of DLL3 may allow for the identification of NEPC in patients in a benign, non-invasive way early enough to better inform clinical decision making.

References:

1. Watson PA, Arora VK, Sawyers CL. Emerging mechanisms of resistance to androgen receptor inhibitors in prostate cancer. *Nat Rev Cancer.* 2015;15:701-711.

2. Bluemn EG, Coleman IM, Lucas JM, et al. Androgen receptor pathway-independent prostate cancer is sustained through FGF signaling. *Cancer Cell.* 2017;32:474-489 e476.

3. Quintanal-Villalonga A, Chan JM, Yu HA, et al. Lineage plasticity in cancer: a shared pathway of therapeutic resistance. *Nat Rev Clin Oncol.* 2020;17:360-371.

4. Davies AH, Beltran H, Zoubeidi A. Cellular plasticity and the neuroendocrine phenotype in prostate cancer. *Nat Rev Urol.* 2018;15:271-286.

5. Ku SY, Rosario S, Wang Y, et al. Rb1 and Trp53 cooperate to suppress prostate cancer lineage plasticity, metastasis, and antiandrogen resistance. *Science.* 2017;355:78-83.

6. Borromeo MD, Savage TK, Kollipara RK, et al. ASCL1 and NEUROD1 reveal heterogeneity in pulmonary neuroendocrine tumors and regulate distinct genetic programs. *Cell Rep.* 2016;16:1259-1272.

7. Owen DH, Giffin MJ, Bailis JM, Smit MD, Carbone DP, He K. DLL3: an emerging target in small cell lung cancer. *J Hematol Oncol.* 2019;12:61.

8. Puca L, Gavyert K, Sailer V, et al. Delta-like protein 3 expression and therapeutic targeting in neuroendocrine prostate cancer. *Sci Transl Med.* 2019;11:eaav0891.

9. Saunders LR, Bankovich AJ, Anderson WC, et al. A DLL3-targeted antibody-drug conjugate eradicates high-grade pulmonary neuroendocrine tumor-initiating cells in vivo. *Sci Transl Med.* 2015;7:302ra136.

10. Sharma SK, Pourat J, Abdel-Atti D, et al. Noninvasive interrogation of DLL3 expression in metastatic small cell lung cancer. *Cancer Res.* 2017;77:3931-3941.

11. Beltran H, Hruszkewycz A, Scher HI, et al. The role of lineage plasticity in prostate cancer therapy resistance. *Clin Cancer Res.* 2019;25:6916-6924.

12. Fox JJ, Gavane SC, Blanc-Autran E, et al. Positron emission tomography/computed tomography-based assessments of androgen receptor expression and glycolytic activity as a prognostic biomarker for metastatic castration-resistant prostate cancer. *JAMA Oncol.* 2018;4:217-224.

13. Schwarzenboeck SM, Rauscher I, Bluemel C, et al. PSMA ligands for PET imaging of prostate cancer. *J Nucl Med.* 2017;58:1545-1552.

14. Bakht MK, Derecichei I, Li Y, et al. Neuroendocrine differentiation of prostate cancer leads to PSMA suppression. *Endocr Relat Cancer.* 2018;26:131-146.

15. Holland JP, Sheh Y, Lewis JS. Standardized methods for the production of high specific-activity zirconium-89. *Nucl Med Biol.* 2009;36:729-739.

16. Sharma SK, Lyashchenko SK, Park HA, et al. A rapid bead-based radioligand binding assay for the determination of target-binding fraction and quality control of radiopharmaceuticals. *Nucl Med Biol.* 2019;71:32-38.

17. Mu P, Zhang Z, Benelli M, et al. SOX2 promotes lineage plasticity and antiandrogen resistance in TP53- and RB1-deficient prostate cancer. *Science.* 2017;355:84-88.

18. You S, Knudsen BS, Erho N, et al. Integrated classification of prostate cancer reveals a novel luminal subtype with poor outcome. *Cancer Res.* 2016;76:4948-4958.

19. Ross-Adams H, Lamb AD, Dunning MJ, et al. Integration of copy number and transcriptomics provides risk stratification in prostate cancer: A discovery and validation cohort study. *EBioMedicine.* 2015;2:1133-1144.

20. Luboldt W, Zophel K, Wunderlich G, Abramyuk A, Luboldt HJ, Kotzerke J. Visualization of somatostatin receptors in prostate cancer and its bone metastases with Ga-68-DOTATOC PET/CT. *Mol Imaging Biol.* 2010;12:78-84.

21. Vargas HA, Kramer GM, Scott AM, et al. Reproducibility and repeatability of semiquantitative (18)F-fluorodihydrotestosterone uptake metrics in castration-resistant prostate cancer metastases: a prospective multicenter study. *J Nucl Med.* 2018;59:1516-1523.

22. Mansfield AS, Hong DS, Hann CL, et al. A phase I/II study of rovalpituzumab tesirine in delta-like 3-expressing advanced solid tumors. *NPJ Precis Oncol.* 2021;5:74.

23. Tully KM, Tendler S, Carter LM, et al. Radioimmunotherapy targeting delta-like ligand 3 in small cell lung cancer. *Clin Cancer Res.* 2021;In Press.

24. Hansson J, Bjartell A, Gadaleanu V, Dizeyi N, Abrahamsson PA. Expression of somatostatin receptor subtypes 2 and 4 in human benign prostatic hyperplasia and prostatic cancer. *Prostate.* 2002;53:50-59.

25. Morichetti D, Mazzucchelli R, Stramazzotti D, et al. Immunohistochemical expression of somatostatin receptor subtypes in prostate tissue from cystoprostatectomies with incidental prostate cancer. *BJU Int.* 2010;106:1072-1080.

26. Cariaga-Martinez AE, Lorenzati MA, Riera MA, et al. Tumoral prostate shows different expression pattern of somatostatin receptor 2 (SSTR2) and phosphotyrosine phosphatase SHP-1 (PTPN6) according to tumor progression. *Adv Urol.* 2009:723831.

27. Hennigs JK, Muller J, Adam M, et al. Loss of somatostatin receptor subtype 2 in prostate cancer is linked to an aggressive cancer phenotype, high tumor cell proliferation and predicts early metastatic and biochemical relapse. *PLoS One.* 2014;9:e100469.

28. Blee AM, Huang H. Lineage plasticity-mediated therapy resistance in prostate cancer. *Asian J Androl.* 2019;21:241-248.

29. Sasaki T, Sugimura Y. The importance of time to prostate-specific antigen (PSA) nadir after primary androgen deprivation therapy in hormone-naive prostate cancer patients. *J Clin Med.* 2018;7.

30. Afshar-Oromieh A, Debus N, Uhrig M, et al. Impact of long-term androgen deprivation therapy on PSMA ligand PET/CT in patients with castration-sensitive prostate cancer. *Eur J Nucl Med Mol Imaging.* 2018;45:2045-2054.

31. Crumbaker M, Khoja L, Joshua AM. AR signaling and the PI3K pathway in prostate cancer. *Cancers (Basel).* 2017;9.

32. Chen R, Li Y, Buttyan R, Dong X. Implications of PI3K/AKT inhibition on REST protein stability and neuroendocrine phenotype acquisition in prostate cancer cells. *Oncotarget.* 2017;8:84863-84876.

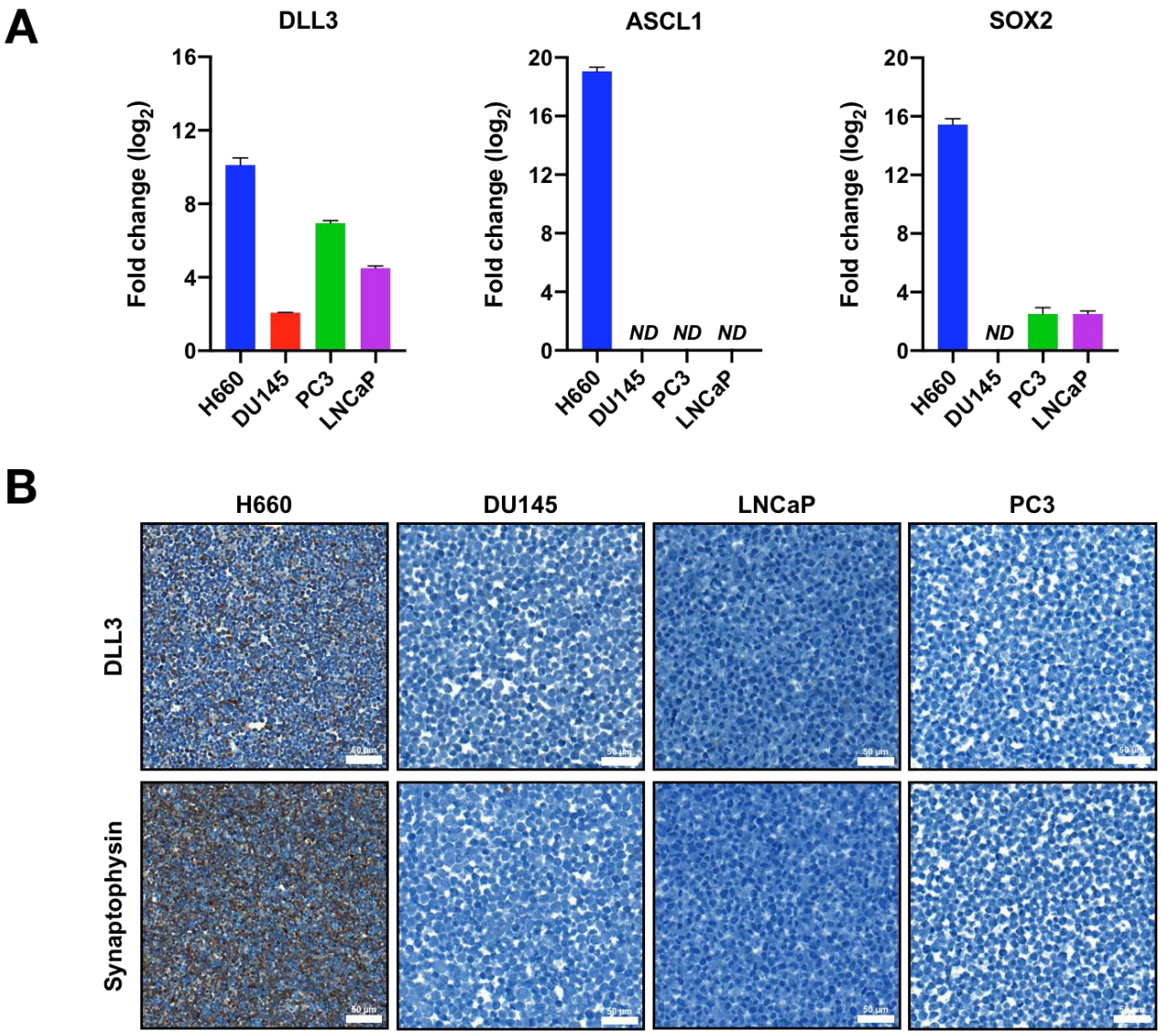

Figure 1. DLL3 is uniquely expressed in H660 cells at the transcriptional and translational level. A. RT-PCR shows the expression patterns of the *DLL3*, *ASCL1*, and *SOX2* genes in H660, DU145, PC3, and LNCaP cells compared to A549 negative control (not shown). *ND*, not detected. **B.** Representative immunohistochemistry images of H660 (DLL3+, SYP+) DU145 (DLL3-/SYP-), LNCaP (DLL3-/SYP-), and PC3 (DLL3-/SYP-) tumor cell sections for DLL3 and SYP. Scale bars, 50 µm.

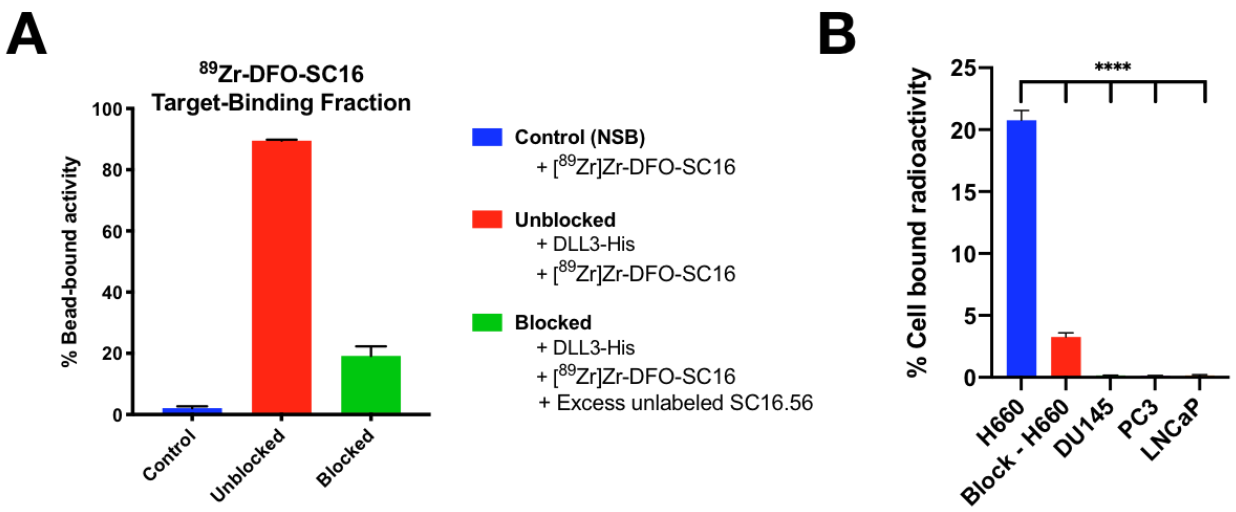

Figure 2. DLL3 is expressed on the cell surface of H660 tumor cells that can be targeted by ^{89}Zr-DFO-SC16. A. ^{89}Zr-DFO-SC16 shows high and specific binding to Ni-NTA beads coated with His-tagged DLL3. Minimum non-specific binding (NSB) is observed (control). Specificity of binding to His-tagged DLL3 was shown in the presence of 5000-fold excess of unlabeled SC16. **B.** *In vitro* cell binding data of ^{89}Zr-DFO-SC16 binding to H660 cells confirms DLL3 expression on the cell surface that can be targeted using our anti-DLL3 mAb SC16. Minimal binding of ^{89}Zr-DFO-SC16 is observed to DLL3-negative DU145, PC3, and LNCaP cells. Specificity of binding to H660 cells was shown in the presence of 1000-fold excess of unlabeled SC16. ****$p < 0.0001$.

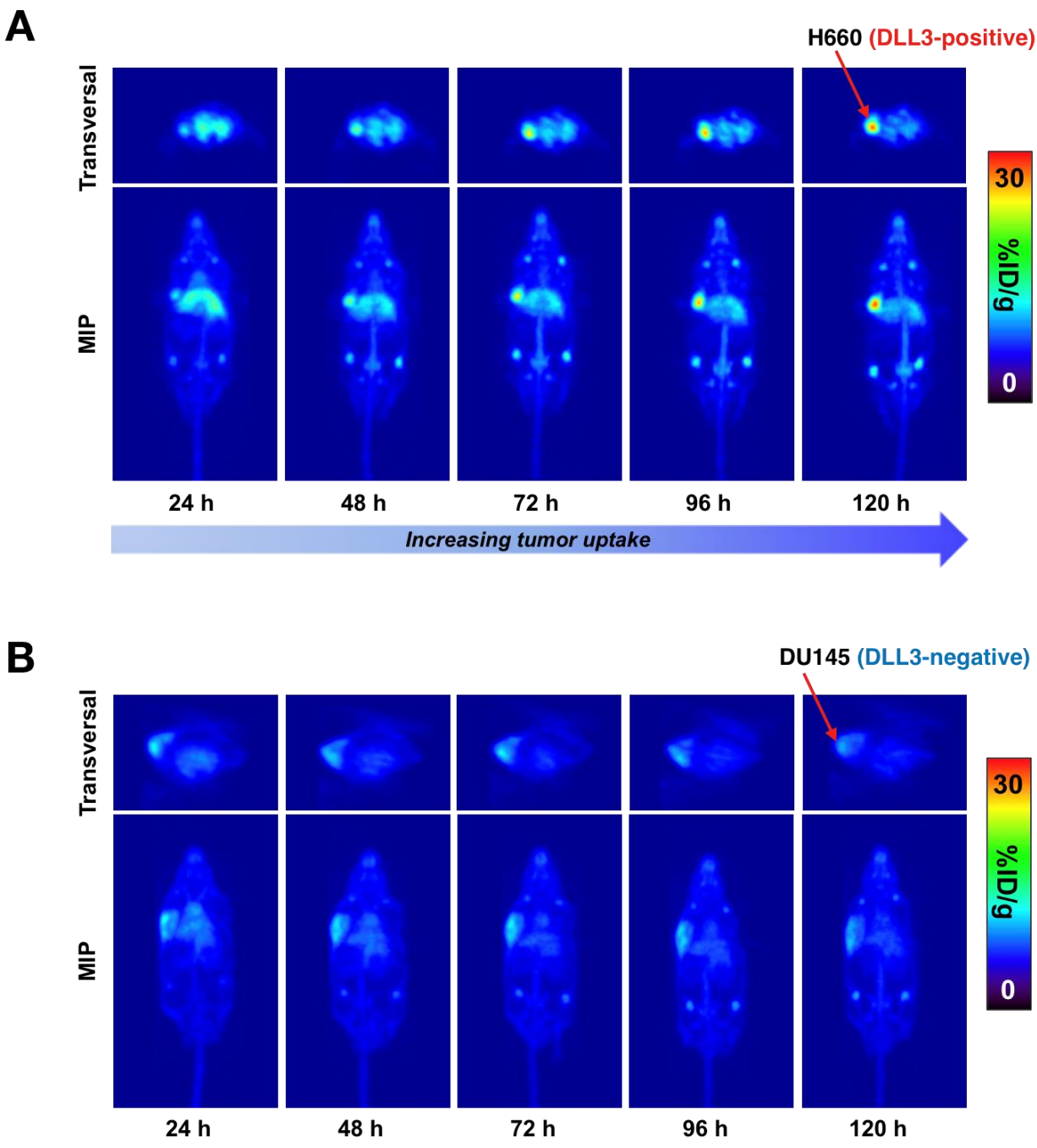

Figure 3. DLL3-expressing subcutaneous H660 tumors could be imaged with ^{89}Zr-DFO-SC16 *in vivo*. A. PET images of ^{89}Zr-DFO-SC16 in an athymic nude male mouse bearing subcutaneous H660 tumor xenografted on the left shoulder. PET imaging was performed at 24 h intervals up to 120 h post-injection of ^{89}Zr-DFO-SC16. **B.** PET images of ^{89}Zr-DFO-SC16 in an athymic nude male mouse bearing subcutaneous DU145 tumor xenografted on the left shoulder.

PET imaging was performed at 24 h intervals up to 120 h post-injection of ^{89}Zr-DFO-SC16. The images represent maximum intensity projection (MIP) and transverse planar images at designated time points after injection of the radiotracer.

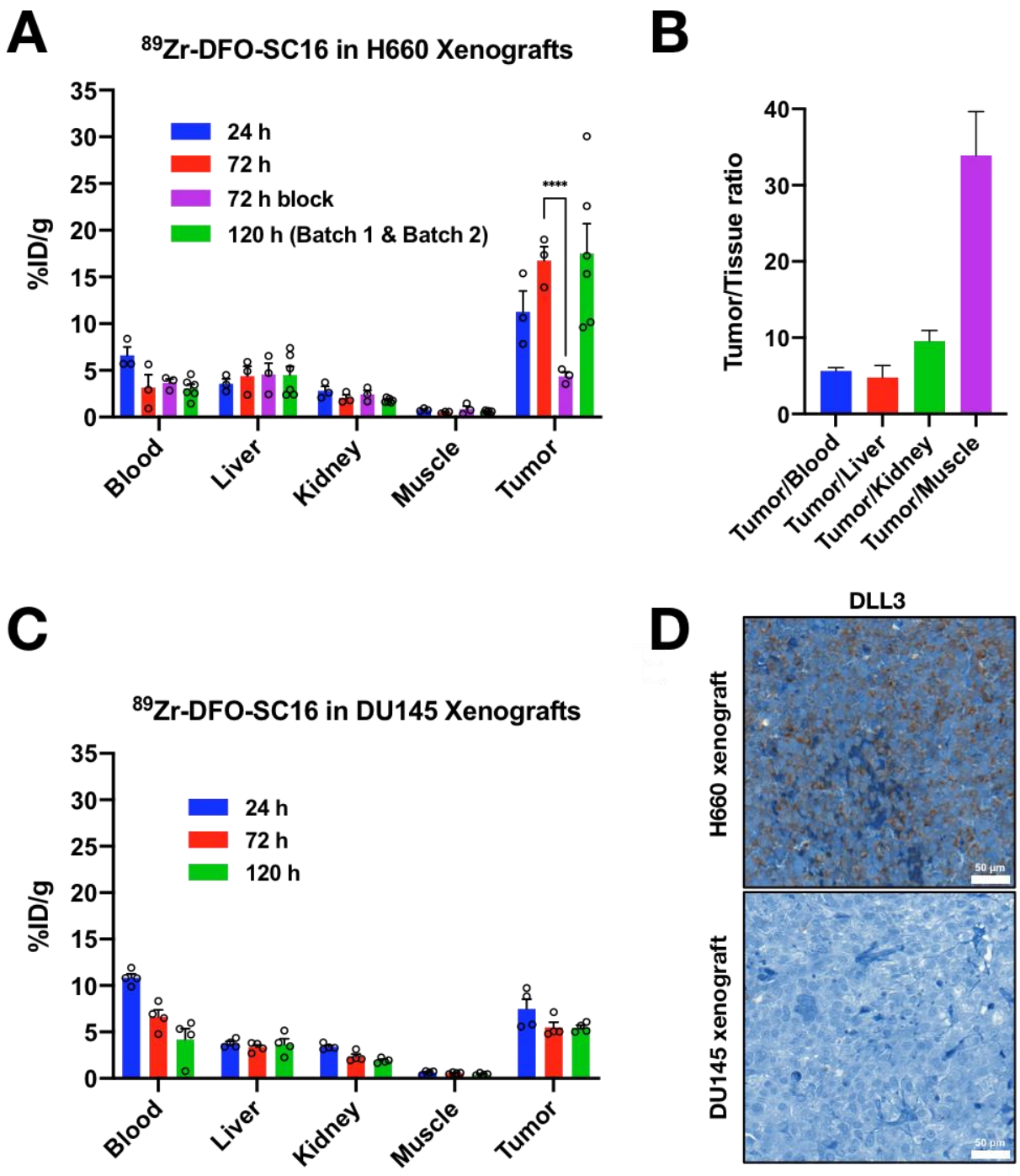

Figure 4. Biodistribution of ^{89}Zr-DFO-SC16 in subcutaneous xenograft model of NEPC

A. Select organ biodistribution data at 24, 72, and 120 h post-intravenous injection of ^{89}Zr-DFO-SC16 in athymic nude mice bearing subcutaneous H660 tumors. Bars at 24 and 72 h represent data obtained from batch #1, n = 3. Bars at 120 h represent data obtained from batch #1 and

batch #2, n = 6. *See Supplementary Information for details on the two different cohorts used in the biodistribution study.* %ID g^{-1}, percentage of injected dose per gram. H660 tumor uptake could be blocked at 72 h post-injection of ^{89}Zr-DFO-SC16 with a 50-fold excess of unlabeled SC16 antibody. ****$p < 0.0001$. **B.** Tumor-to-background contrast ratios from the uptake of ^{89}Zr-DFO-SC16 in H660 xenograft bearing mice. **C.** Select organ biodistribution at 24, 72, and 120 h post-injection of ^{89}Zr-DFO-SC16 in athymic nude mice bearing subcutaneous DU145 tumors. **D.** Representative immunohistochemistry images of H660 and DU145 subcutaneous tumor xenografts for DLL3. Scale bars, 50 μm.

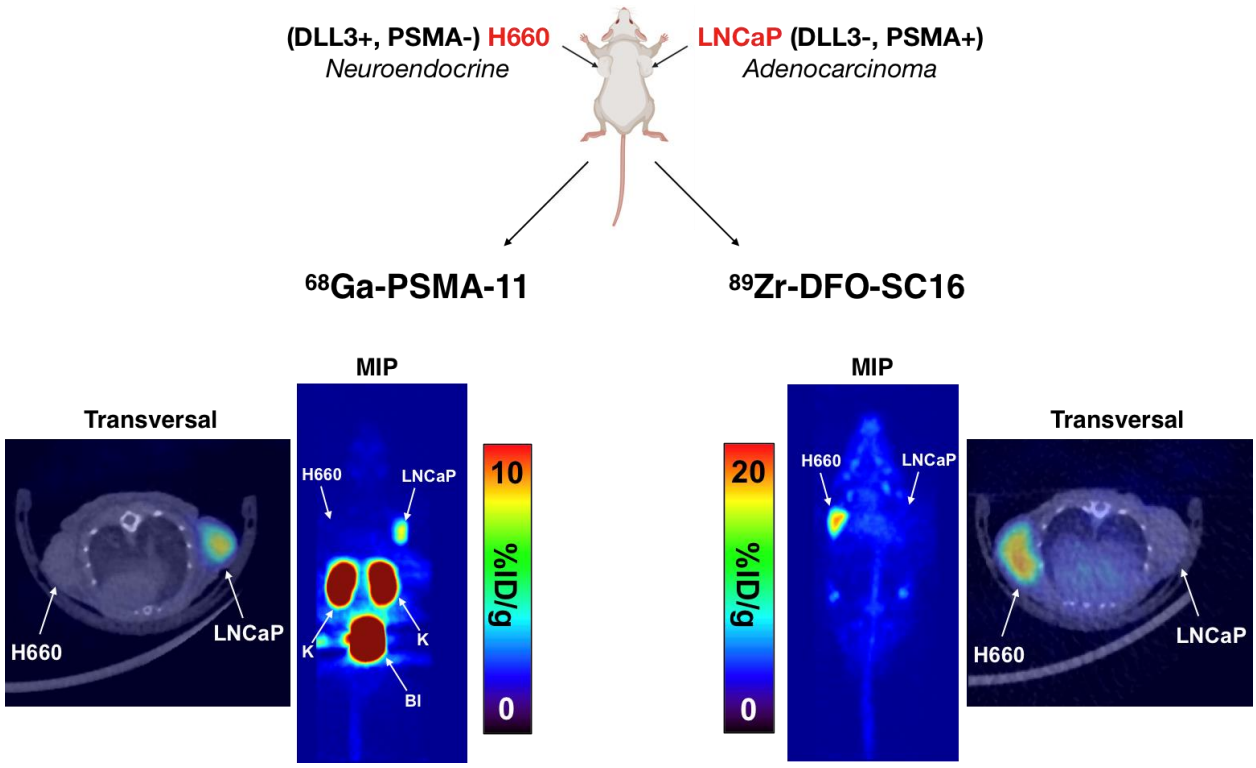

Figure 5. ^{68}Ga-PSMA-11 cannot image NEPC lesions *in vivo*. PET images of ^{68}Ga-PSMA-11 (1 h post-injection) or ^{89}Zr-DFO-SC16 (120 h post-injection) in an athymic nude male mouse bearing H660 and LNCaP tumors xenografted on the left and right shoulder, respectively.

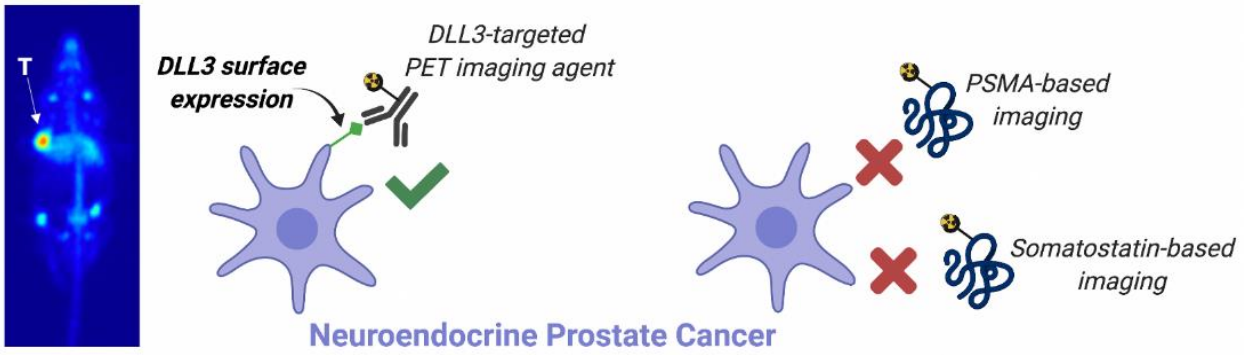

Graphical Abstract

SUPPLEMENTARY MATERIALS

Cell lines

All cell lines were obtained from the American Type Culture Collection. Cultures were grown in aseptic conditions at 37 ºC and 5% CO_2 in a humidified atmosphere. NCI-H660 cells were grown in DMEM/F12 medium supplemented with 10% fetal bovine serum, 10 nM beta-estradiol, 10 nM hydrocortisone, 30 nM sodium selenite, 0.005 mg/mL insulin, 0.01 mg/mL transferrin, 4 mM L-glutamine, 100 units/mL penicillin, and 100 µg/mL streptomycin. DU145 cells were grown in DMEM medium supplemented with 10% fetal bovine serum, 100 units/mL penicillin, and 100 µg/mL streptomycin. LNCaP cells were grown in RPMI-1640 medium supplemented with 10% fetal bovine serum, 100 units/mL penicillin, and 100 µg/mL streptomycin. H82 cells were cultured in RPMI-1640 medium supplemented with 10% fetal bovine serum, 2 mM L-glutamine, 10 mM HEPES, 1 mM sodium pyruvate, 4.5 g/L glucose, 1.5 g/L sodium bicarbonate, 100 units/mL penicillin, and 100 µg/mL streptomycin. PC3 cells were grown in F-12 Kaighn's medium supplemented with 10% fetal bovine serum, 100 units/mL penicillin, and 100 µg/mL streptomycin.

RNA isolation and quantitative real-time PCR

Approximately 5 million cells were pelleted and washed with PBS before proceeding to RNA extraction. RNA extraction from cell pellets was done using RNeasy mini kit (QIAGEN). On column DNA digestion was done using RNase-Free DNase set (QIAGEN). RNA quality and quantity were determined using a spectrophotometer at 260 and 280 nm (Nanodrop-2000, Thermo Scientific). cDNA was generated using the High Capacity cDNA Reverse Transcription Kit (Applied Biosystems; Life Technologies). Quantitative-PCR was performed using RT^2

SYBR Green Fluor qPCR Mastermix and RT^2 qPCR primers (Qiagen) on a CFX96 Touch Real-Time PCR Detection System (Bio Rad). *DLL3*, *ASCL1*, *SOX2*, *AR*, *FOLH1 (PSMA)*, and *KLK3 (PSA)* expression were quantified relative to beta actin using the comparative CT method. Log_2 fold changes were calculated by comparing expression levels to negative control H82 and A549 human lung cancer cell lines.

Synthesis of ^{89}Zr-DFO-SC16

The DFO-SC16 (or DFO-IgG control) was produced by the incubation of SC16 with a 6-molar excess of the chelator *p*-isothiocyanatobenzoyl desferrioxamine (*p*-SCN-DFO, Macrocyclics, Inc.) at a pH of 9 and 25 ºC for 90 min on a thermomixer. The immunoconjugates were purified by size exclusion chromatography on a PD-10 desalting column (GE Healthcare) and concentrated with a 50,000 MWCO Amicon centrifugal filter. Zirconium-89 (^{89}Zr) was produced by the proton bombardment of ^{89}Y foil on a cyclotron and supplied by the Radiochemistry & Molecular Imaging Probes core at Memorial Sloan Kettering Cancer Center. The ^{89}Zr-oxalate solution (5.55 MBq) was adjusted to pH 6.5–7.0 by addition of 1 M sodium carbonate (Na_2CO_3) and incubated at room temperature with the DFO-mAbs (15 μg) for 1 hour on a thermomixer. The ^{89}Zr-DFO-mAbs were purified on a PD-10 desalting column and radiochemical purity was assessed by radio-instant thin layer chromatography (radio-iTLC) using 50 mM ethylenediaminetetraacetic acid (EDTA) as the eluent. The radioimmunoconjugate stability and demetallation of ^{89}Zr was evaluated in an *in vitro* serum stability assay by incubating ^{89}Zr-DFO-SC16 in human serum at 37 ºC for 5 days. Radiochemical purity and demetallation of ^{89}Zr were determined via radio-iTLC.

In vitro bead-based binding assay

To determine the DLL3 target-binding fraction of ^{89}Zr-DFO-SC16, a bead-based radioligand binding assay was performed using magnetic beads functionalized with His-tagged DLL3 protein (R&D Systems). For the control, the procedure was the same except no His-tagged DLL3 was added to assess non-specific binding of ^{89}Zr-DFO-SC16 to the magnetic beads alone. For the block, the procedure was the same except 5 µg of DFO-SC16 was also added to determine specificity of ^{89}Zr-DFO-SC16 binding to His-tagged DLL3.

In vitro saturation binding assay

A 0.15 µg/mL solution of ^{89}Zr-DFO-SC16 was prepared in PBS with 1% BSA. 3 ng (20 µL) of the radiolabeled construct was added to an Eppendorf tube containing 10x10^6 cells in 0.2 mL of culture media. The mixture was allowed to incubate for 1 hour with intermittent pipetting up/down every 15 minutes to resuspend the cells. Next, the cells were centrifuged (600 x g for 5 min) followed by pipetting out the media supernatant to another centrifuge tube. Then, the cells were washed with 1 mL of ice-cold PBS, centrifuged (600 x g for 5 min), and the PBS supernatant was pipetted out into a separate Eppendorf tube. The washing procedure was repeated two more times. Lastly, the cell pellet, the media supernatant, and the three wash fractions were placed on a gamma counter to determine the percent of cell bound radioactivity of the radiolabeled construct. The above procedure was repeated for a 0.15 µg/mL solution of ^{89}Zr-DFO-IgG in PBS with 1% BSA.

Immunohistochemistry

The immunohistochemistry detection of AR, DLL3, Synaptophysin, and PSMA were performed at Molecular Cytology Core Facility of Memorial Sloan Kettering Cancer Center, using Discovery XT processor (Ventana Medical Systems, Roche - AZ). After 32 min of heat and CC1 (Cell Conditioning 1, Ventana catalog#: 950-500) retrieval, the tissue sections were blocked first for 30 min in Background Blocking reagent (Innovex, catalog#: NB306).

A rabbit monoclonal anti-AR antibody (Epitomics, catalog#: 3184-1) was used in 0.66 µg/mL concentration. The incubation with the primary antibody was done for 5 h, followed by 60 min incubation with biotinylated goat anti-rabbit IgG (Vector labs, catalog#: PK6101) in 5.75 µg/mL. Blocker D, Streptavidin- HRP and DAB detection kit (Ventana Medical Systems) were used according to the manufacturer instructions. The slides were counterstained with hematoxylin and coverslipped with Permount (Fisher Scientific).

A rabbit monoclonal anti-DLL3 antibody (Ventana Ref#: 790-7016) was used in prediluted ready to use concentration. The incubation with the primary antibody was done for 4 h, followed by 60 min incubation with biotinylated goat anti-rabbit IgG (Vector labs, catalog#: PK6101) in 5.75 µg/mL, followed by application of Blocker D, Streptavidin- HRP and DAB detection kit (Ventana Medical Systems), according to the manufacturer instructions. The slides were counterstained with hematoxylin and coverslipped with Permount (Fisher Scientific).

A rabbit monoclonal anti-Synaptophysin antibody (Epitomics, catalog#: 1485) was used in 0.05 µg/mL concentration. The incubation with the primary antibody was done for 6 h, followed by 60 min with biotinylated goat anti-rabbit IgG (Vector labs, catalog#: PK6101) in 5.75 µg/mL. Blocker D, Streptavidin- HRP and DAB detection kit (Ventana Medical Systems)

were used according to the manufacturer instructions. The slides were counterstained with hematoxylin and coverslipped with Permount (Fisher Scientific).

A rabbit polyclonal anti-PSMA antibody (Proteintech, catalog#: 13163-1-AP) was used in 1 µg/mL concentration. The incubation with the primary antibody was done for 5 h, followed by 60 min incubation with biotinylated goat anti-rabbit IgG (Vector labs, catalog#: PK6101) in 5.75 µg/mL. Blocker D, Streptavidin- HRP and DAB detection kit (Ventana Medical Systems) were used according to the manufacturer instructions. The slides were counterstained with hematoxylin and coverslipped with Permount (Fisher Scientific).

Subcutaneous xenograft model

To develop the subcutaneous xenograft models, 6–8-week-old male athymic nude mice were injected subcutaneously on the left shoulder with 5 million H660 cells or DU145 cells in 1:1 media/matrigel basement membrane matrix (BD Biosciences). To generate the dual subcutaneous xenograft model, 6-8 week old male athymic nude mice were injected with 5 million H660 cells subcutaneously on the left shoulder and with 5 million LNCaP cells on the right shoulder in 1:1 media/matrigel basement membrane matrix. The tumors were allowed to grow for 3–5 weeks, and then the mice were used for PET imaging and biodistribution studies.

Biodistribution Studies

For biodistribution studies, mice were warmed under a heat lamp prior to administration of the radioimmunoconjugates (1.00–3.80 MBq; 2.7–10.3 µg in 200 µL chelexed PBS for H660 tumors) (0.32–0.98 MBq; 0.87–2.7 µg in 200 µL chelexed PBS for DU145 tumors) via intravenous tail vein injection (t = 0). Mice were euthanized by CO_2 asphyxiation at 24, 72, and

120 h post tracer administration. For the blocking study, a co-injection of ^{89}Zr-DFO-SC16 (0.94–0.97 MBq; 2.55–2.63 μg in 200 μL chelexed PBS) and 50-fold excess of cold, unlabeled SC16 was injected into the mice and then euthanized at 72 h post-injection. Non-specific uptake in DLL3-positive H660 subcutaneous xenografts was determined by injection with ^{89}Zr-DFO-IgG (3.60-3.70 MBq; 9.7–10.0 μg in 150 μL chelexed PBS) and then euthanized at 120 h post-injection. After asphyxiation, organs of interest and the tumor were harvested, weighed, and counted on a gamma-counter to determine accumulation of radioactivity. The mass of the injected radioimmunoconjugates were measured and compared to a standard syringe of known activity and mass to determine the total number of counts injected per mouse. The percent injected dose per gram (%ID/g) was determined for each sample by normalizing the counts per sample to the total amount of activity injected.

PET/CT Imaging

Mice bearing H660 subcutaneous tumors were intravenously injected with ^{89}Zr-DFO-SC16 (3.60–3.80 Mbq; 9.7–10.3 μg in 150 μL chelexed PBS) or ^{89}Zr-DFO-IgG (3.60–3.70 MBq; 9.7–10.0 μg in 150 μL chelexed PBS) or ^{68}Ga-DOTA-TATE (7.66–8.33 Mbq in 150 μL formic acid, sodium hydroxide, and sterile water solution). Mice bearing DU145 subcutaneous tumors were intravenously injected with ^{89}Zr-DFO-SC16 (5.85–6.22 MBq; 15.8–16.8 μg in 150 μL chelexed PBS). Mice bearing dual LNCaP and H660 tumors were intravenously injected with ^{89}Zr-DFO-SC16 (4.42–4.62 Mbq; 11.9–12.5 μg in 150 μL chelexed PBS) and ^{68}Ga-PSMA-11 (8.66–8.92 Mbq in 150 μL sterile acetate buffer). Mice were anesthetized with 1–2% isoflurane and images were acquired from an Inveon microPET/CT instrument (Siemens).

Supplementary Figures:

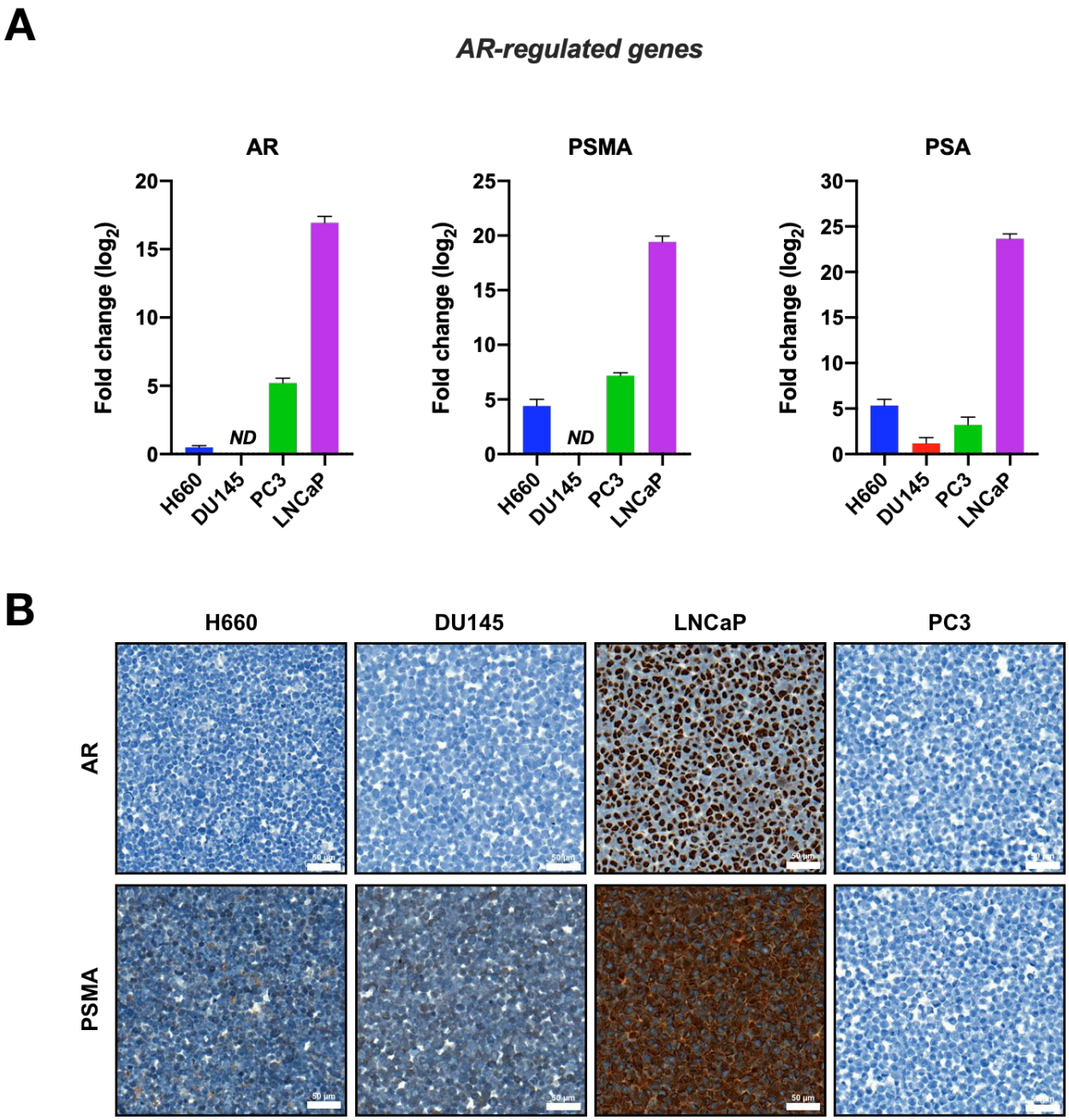

Figure 1. AR, PSMA, and PSA are absent in H660 cells at the transcriptional and translational level. A. RT-PCR shows the expression patterns of the *AR* gene (*AR*), *PSMA* gene (*FOLH1*), and *PSA* gene (*KLK3*) in DU145, PC3, H660, and LNCaP cells compared to A549 (*PSMA* and *PSA*) and H82 (*AR*) negative controls (not shown). *ND*, not detected **B.**

Representative immunohistochemistry images of H660 (AR-/PSMA-), DU145 (AR-/PSMA-), LNCaP (AR+/PSMA+), and PC3 (AR-/PSMA-) tumor cell sections for AR and PSMA. Scale bars, 50 μm.

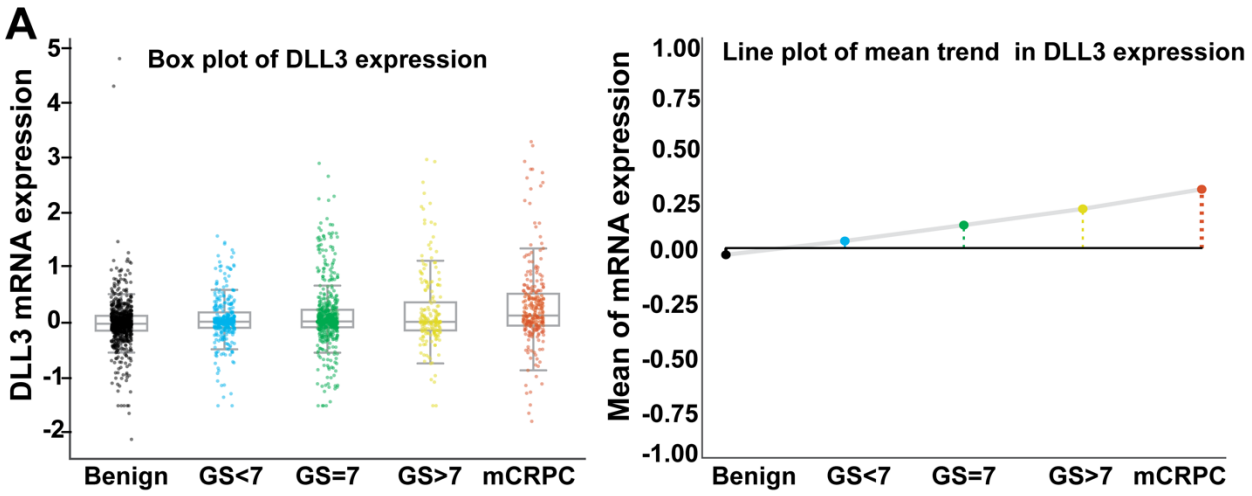

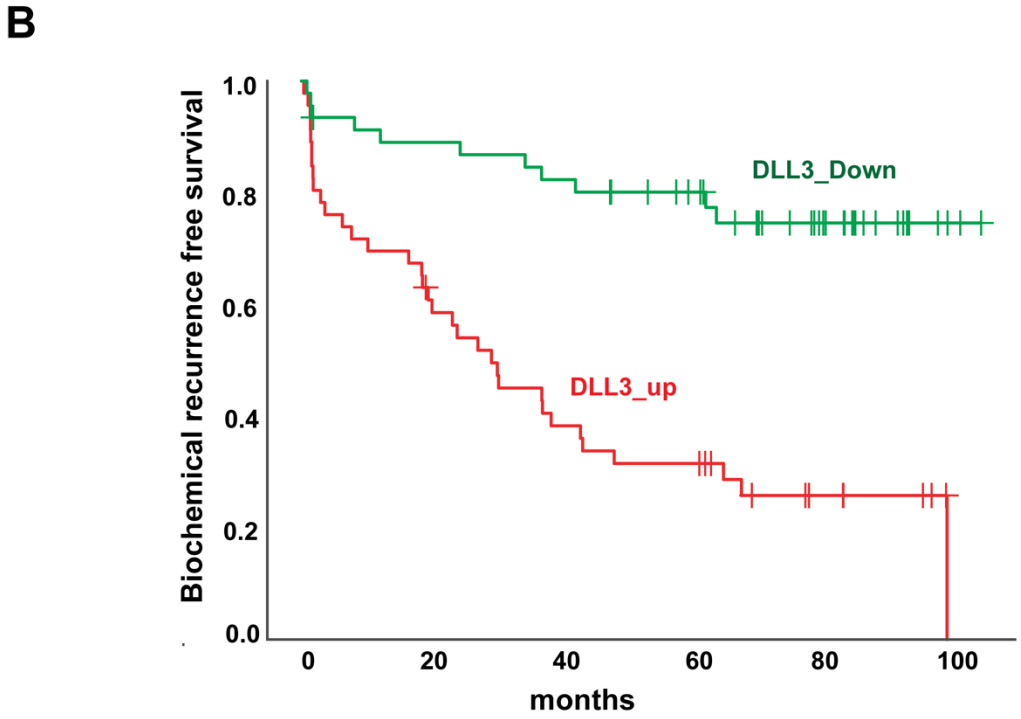

Supplementary Figure 2. Overexpression of *DLL3* associated with prostate cancer progression. A. The box plot showing the upregulation of *DLL3* mRNA expression in advanced prostate cancer (Left). The line plot showing the mean trend of *DLL3* mRNA expression in various grades and stages of prostate cancer (Right). The graphs were generated using Prostate Cancer Transcriptome Atlas and p-value between groups was determined by one way ANOVA. One-way ANOVA test between subsets: F-value = 14.030, P-value = <0.001; Ranksums-test

between subsets (mCRPC VS Primary): Fold change = 0.179, P-value = <0.001; Ranksums-test between subsets (Primary VS Benign): Fold change = 0.133, P-value = <0.001 **B.** Disease/progression-free survival (probability of freedom from biochemical recurrence) according to *DLL3* mRNA expression status among patients in the Ross-Adams *et al*. prostate cancer cohort (GSE70769). Log-rank test was used to compare groups. Survival curve and cox potential hazard regression analysis were performed using Prostate Cancer Transcriptome Atlas.

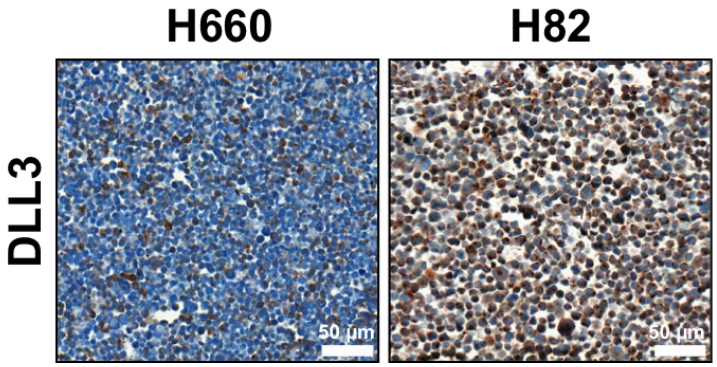

Supplementary Figure 3. Representative immunohistochemistry images of H660 and H82 tumor cell sections for DLL3. Scale bars, 50 µm.

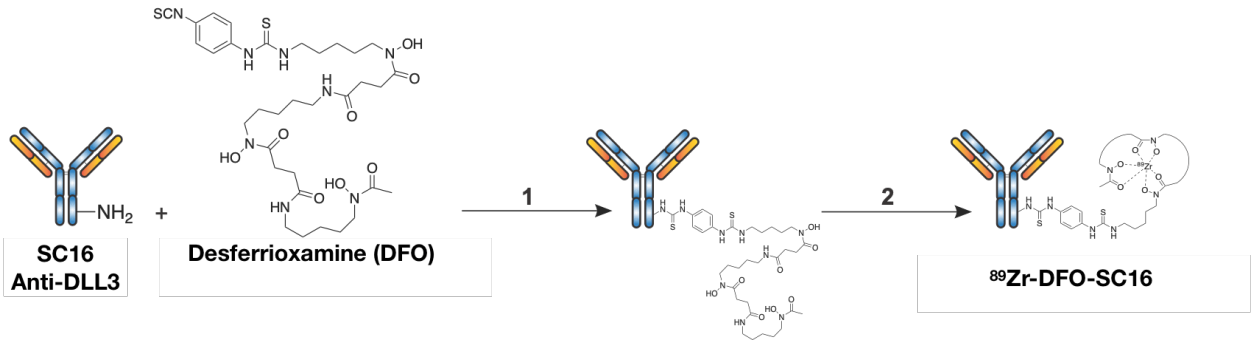

Supplemental Figure 4. Overview of the synthesis of ^{89}Zr-DFO-SC16. Schematic representation of ^{89}Zr-DFO-SC16 preparation showing DFO conjugation to SC16 and then radiolabeling of the DFO-SC16 construct. (1) PBS/Na_2CO_3, pH 9.0, 37 ºC, 90 min; (2) ^{89}Zr-oxalate, pH 6.8; PBS, RT, 1h.

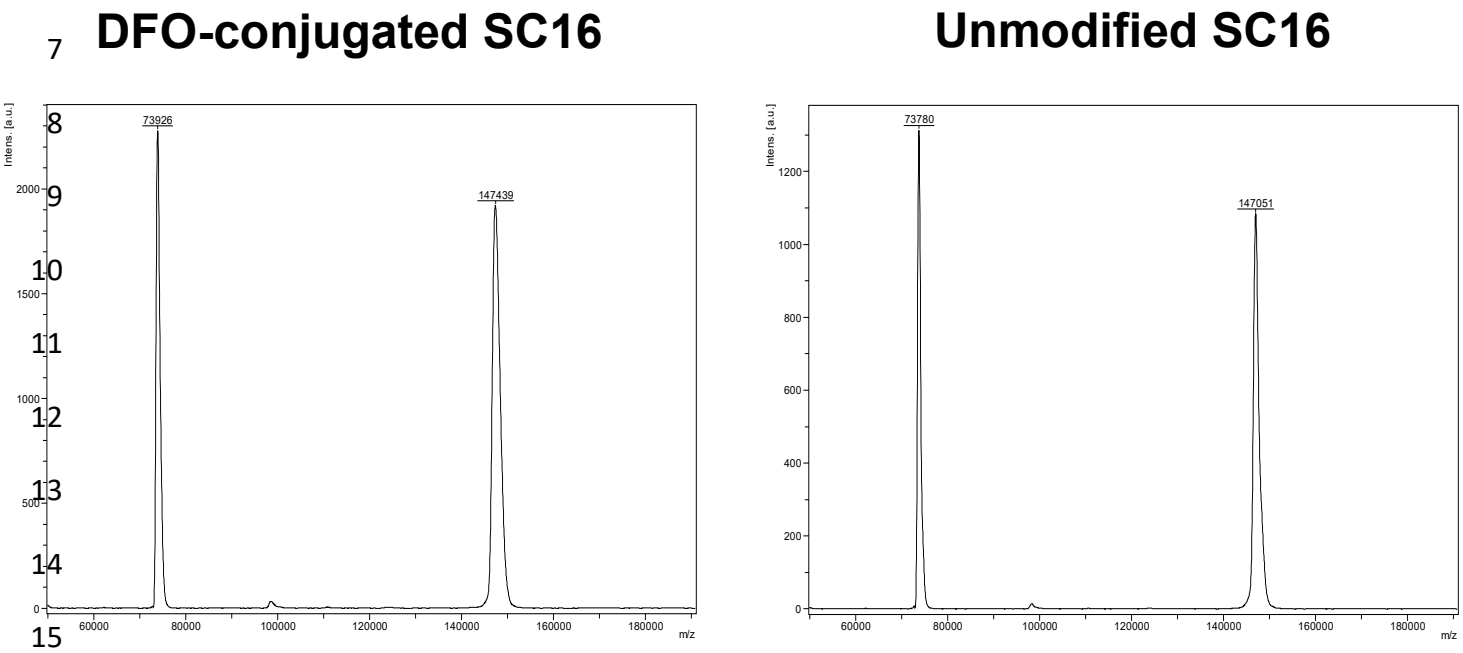

Supplemental Figure 5. MALDI-TOF spectra of the unmodified SC16 and the DFO-conjugated SC16. Representative spectra show a peak corresponding to the mass of the unmodified SC16 antibody (MW ~ 147051) and peak corresponding to the DFO-conjugated SC16 antibody (MW ~147439). Analysis revealed an average of 0.44 DFOs conjugated to SC16.

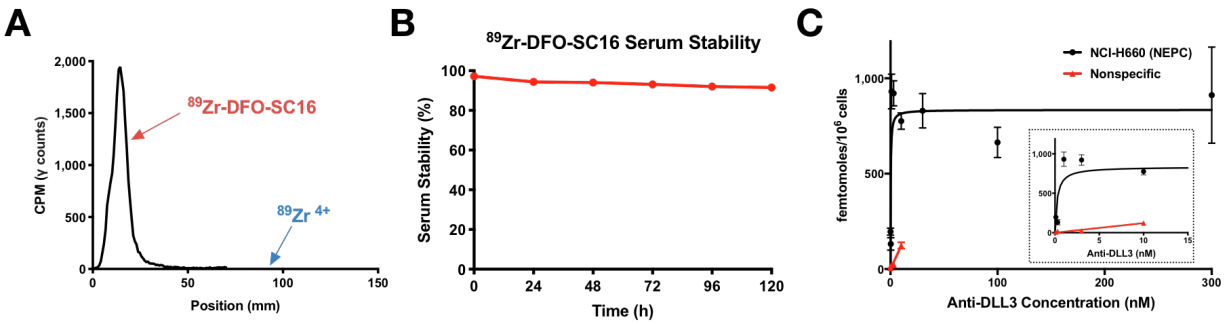

Supplemental Figure 6. A. Radio-iTLC of ^{89}Zr-DFO-SC16 after purification by PD-10 column. High radiochemical purity (> 99%) was achieved. **B.** The purified ^{89}Zr-DFO-SC16 was incubated in human serum at 37 ºC. Stability of the construct, as determined by radio-iTLC, was shown to be > 92% stable over a 5-day period. **C.** A plot of the saturation binding curve of ^{89}Zr-DFO-SC16 to H660 cells. Data analysis performed using PRISM revealed values for B_{max} = 862.6 ± 55.5 femtomoles/10^6 cells and K_d < 1 nM.

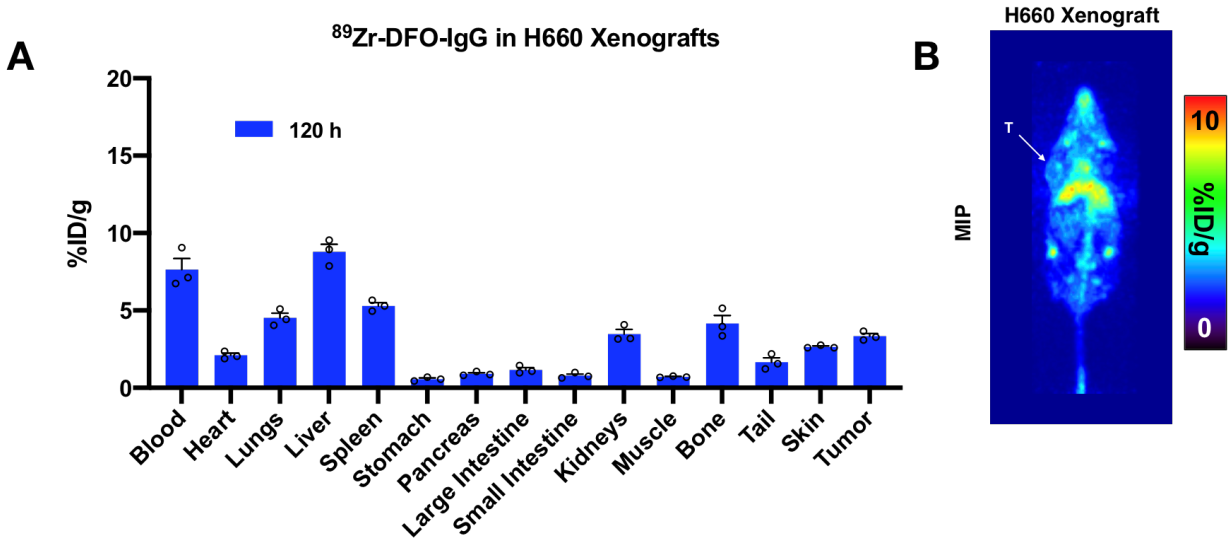

C

Time	120 h (n = 3)
	%ID/g ± SEM
Blood	7.64 ± 0.72
Heart	2.10 ± 0.14
Lungs	4.52 ± 0.30
Liver	8.79 ± 0.49
Spleen	5.30 ± 0.20
Stomach	0.56 ± 0.07
Pancreas	0.91 ± 0.07
Large Intestine	1.16 ± 0.14
Small Intestine	0.79 ± 0.10
Kidneys	3.47 ± 0.30
Muscle	0.71 ± 0.02
Bone	4.16 ± 0.52
Tail	1.66 ± 0.28
Skin	2.65 ± 0.06
Tumor	3.34 ± 0.17

Supplemental Figure 7. Full biodistribution data and imaging of ^{89}Zr-DFO-IgG after lateral tail vein injection in H660 subcutaneous xenograft bearing mice. **A.** Percent injected dose per gram of tissue after five days. **B.** Maximum intensity projection (MIP) of ^{89}Zr-DFO-IgG in male nude mouse xenografted with H660 tumor on the left shoulder. **C.** Tabulated biodistribution data expressed as mean %ID/g ± SEM.

A

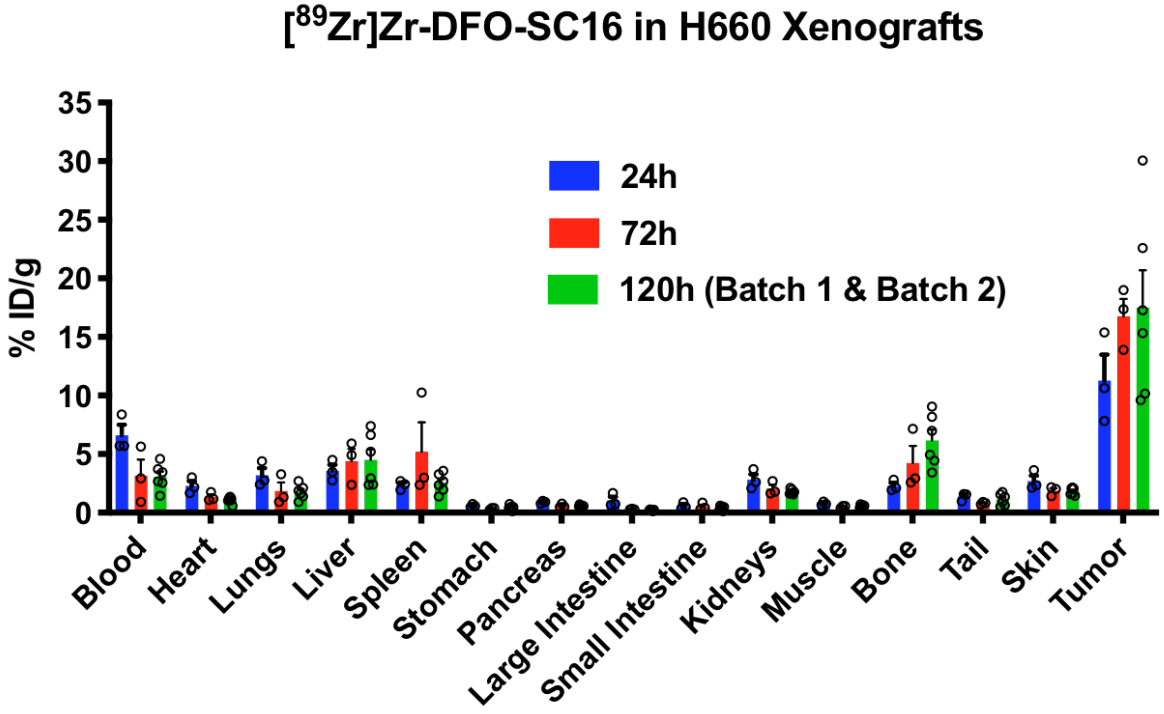

B

Time	24 h (n = 3)	72 h (n = 3)	120 h (n = 6)
	%ID/g ± SEM	%ID/g ± SEM	%ID/g ± SEM
Blood	6.60 ± 0.90	3.16 ± 1.37	3.07 ± 0.45
Heart	2.30 ± 0.39	1.35 ± 0.21	1.08 ± 0.11
Lungs	3.19 ± 0.61	1.84 ± 0.73	1.78 ± 0.25
Liver	3.58 ± 0.50	4.40 ± 1.05	4.50 ± 0.91
Spleen	2.36 ± 0.22	5.20 ± 2.53	2.55 ± 0.33
Stomach	0.60 ± 0.08	0.35 ± 0.04	0.45 ± 0.08
Pancreas	0.90 ± 0.07	0.59 ± 0.09	0.55 ± 0.05
Large Intestine	1.03 ± 0.33	0.30 ± 0.02	0.23 ± 0.02
Small Intestine	0.58 ± 0.16	0.53 ± 0.17	0.39 ± 0.07
Kidneys	2.81 ± 0.48	2.05 ± 0.32	1.78 ± 0.09
Muscle	0.78 ± 0.08	0.51 ± 0.06	0.54 ± 0.06
Bone	2.29 ± 0.26	4.23 ± 1.47	6.17 ± 0.91
Tail	1.37 ± 0.20	0.82 ± 0.06	1.12 ± 0.21
Skin	2.70 ± 0.46	1.87 ± 0.22	1.83 ± 0.13
Tumor	11.28 ± 2.21	16.75 ± 1.51	17.50 ± 3.19

Supplemental Figure 8. Full biodistribution data of ^{89}Zr-DFO-SC16 after lateral tail vein injection in H660 subcutaneous xenograft bearing mice. **A.** Percent injected dose per gram of tissue over five days. **B.** Tabulated biodistribution data expressed as mean %ID/g ± SEM.

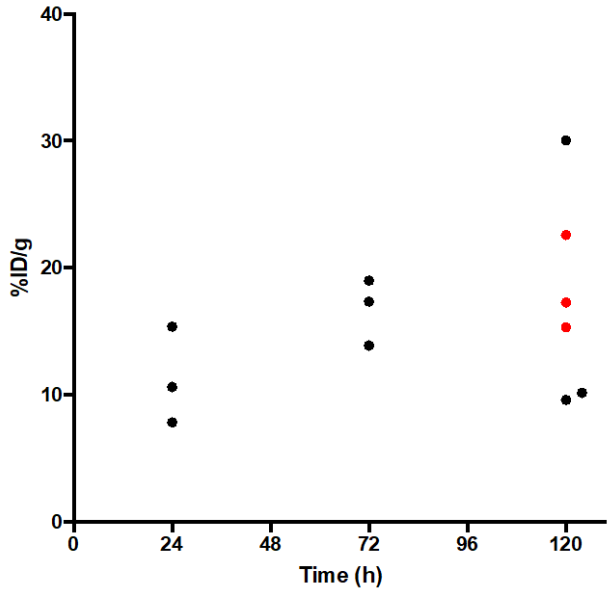

Supplemental Figure 9. ^{89}Zr-DFO-SC16 accumulation at the tumor site increases overtime. Antibody-tumor accumulation at 24, 72, and 120 h post-intravenous injection of ^{89}Zr-DFO-SC16 in athymic nude mice bearing subcutaneous H660 tumors. Data points in black color represent data obtained from batch #1 containing n = 3 mice per group. Because the data obtained at 120 h was slightly different among the 3 mice, we repeated the study for this time-point using batch #2 containing another n = 3 mice per group. Mice from batch #2 were also used for imaging studies shown in Figures 4A and supplemental figure 3. Statistical analyses were performed using Rstudio to account for batch effects determining a correlation between X (time after antibody administration) and Y (%ID/g) and accounting for the extraneous variable Z (mice cohort). Regardless of having data obtained from 2 different mice cohorts, we observed a positive correlation (as determined by linear regression analyses) between X and Y ($P = 0.00971$).

A

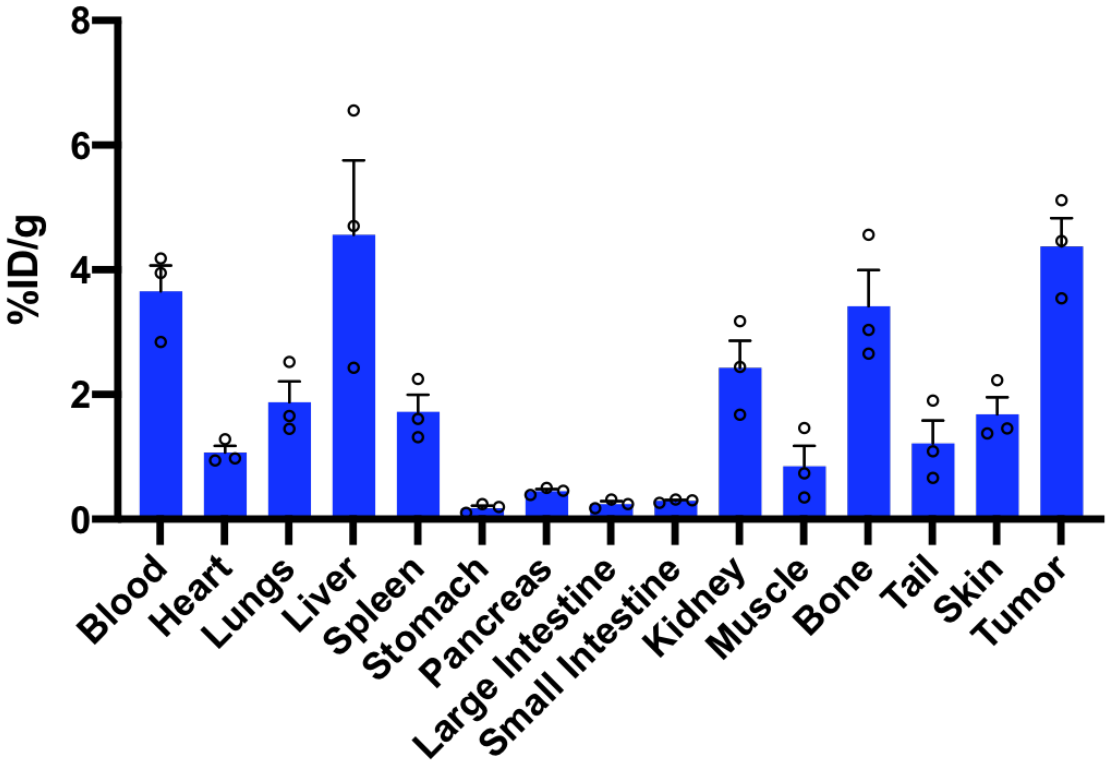

B

Time	72 h Block (n = 3)
	%ID/g ± SEM
Blood	2.63 ± 0.71
Heart	0.79 ± 0.14
Lungs	1.31 ± 0.26
Liver	2.85 ± 0.33
Spleen	1.23 ± 0.14
Stomach	0.14 ± 0.05
Pancreas	0.36 ± 0.02
Large Intestine	0.16 ± 0.02
Small Intestine	0.18 ± 0.03
Kidneys	1.62 ± 0.15
Muscle	0.58 ± 0.16
Bone	2.55 ± 0.46
Tail	0.78 ± 0.15
Skin	1.20 ± 0.17
Tumor	3.01 ± 0.36

Supplemental Figure 10. Full biodistribution data of ^{89}Zr-DFO-SC16 with a 50-fold excess of

cold, unlabeled SC16 antibody after lateral tail vein injection in H660 subcutaneous xenograft bearing mice. **A.** Percent injected dose per gram of tissue 72 h post-injection. **B.** Tabulated biodistribution data expressed as mean %ID/g ± SEM.

A

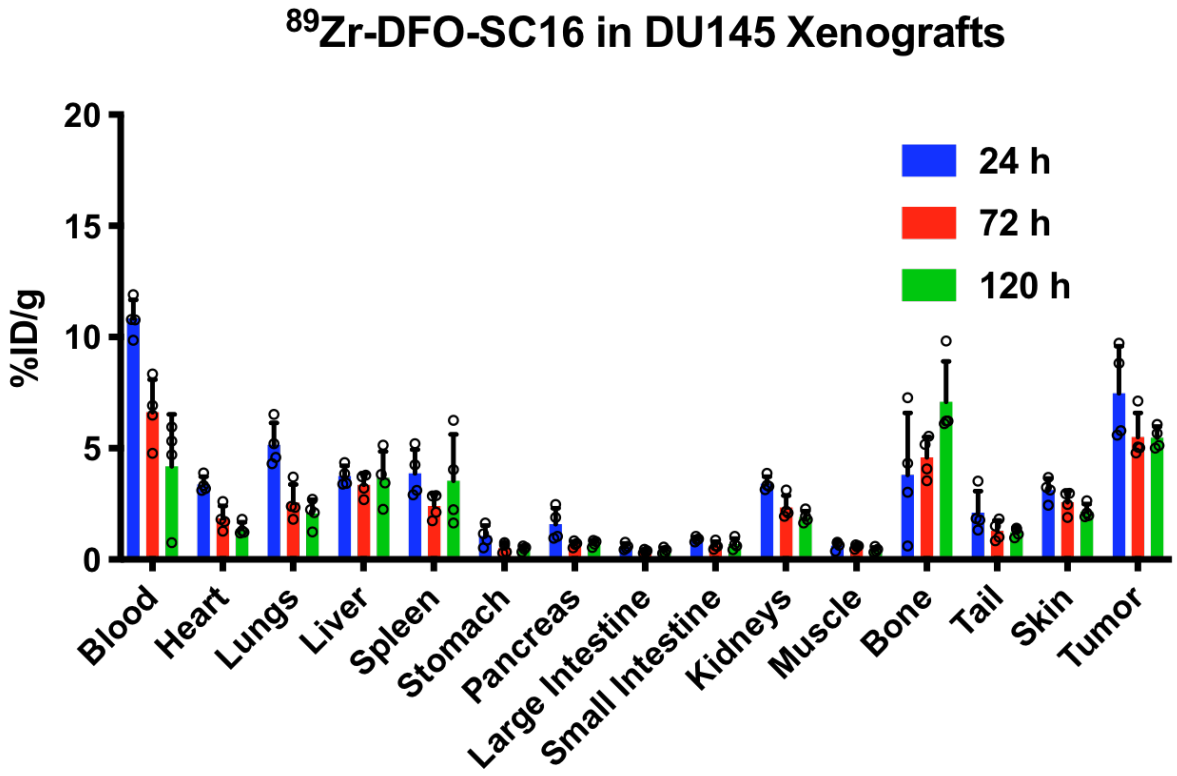

B

Time	24 h (n = 4)	72 h (n = 4)	120 h (n = 4)
	%ID/g ± SEM	%ID/g ± SEM	%ID/g ± SEM
Blood	10.84 ± 0.42	6.63 ± 0.73	4.19 ± 1.17
Heart	3.38 ± 0.18	1.85 ± 0.28	1.38 ± 0.14
Lungs	5.16 ± 0.49	2.56 ± 0.40	2.08 ± 0.31
Liver	3.76 ± 0.23	3.36 ± 0.26	3.67 ± 0.59
Spleen	3.87 ± 0.54	2.40 ± 0.28	3.55 ± 1.04
Stomach	1.05 ± 0.24	0.51 ± 0.11	0.49 ± 0.06
Pancreas	1.59 ± 0.36	0.69 ± 0.06	0.72 ± 0.07
Large Intestine	0.58 ± 0.07	0.37 ± 0.04	0.39 ± 0.06
Small Intestine	0.91 ± 0.05	0.63 ± 0.09	0.69 ± 0.13
Kidneys	3.41 ± 0.16	2.33 ± 0.27	1.92 ± 0.13
Muscle	0.63 ± 0.09	0.57 ± 0.04	0.44 ± 0.06
Bone	3.81 ± 1.39	4.58 ± 0.47	7.10 ± 0.91
Tail	2.12 ± 0.48	1.30 ± 0.23	1.22 ± 0.10
Skin	3.12 ± 0.26	2.58 ± 0.25	2.16 ± 0.16
Tumor	7.48 ± 1.05	5.50 ± 0.54	5.47 ± 0.25

Supplemental Figure 11. Full biodistribution data of ^{89}Zr-DFO-SC16 after lateral tail vein injection in DU145 subcutaneous xenograft bearing mice. **A.** Percent injected dose per gram of tissue over five days. **B.** Tabulated biodistribution data expressed as mean %ID/g ± SEM.

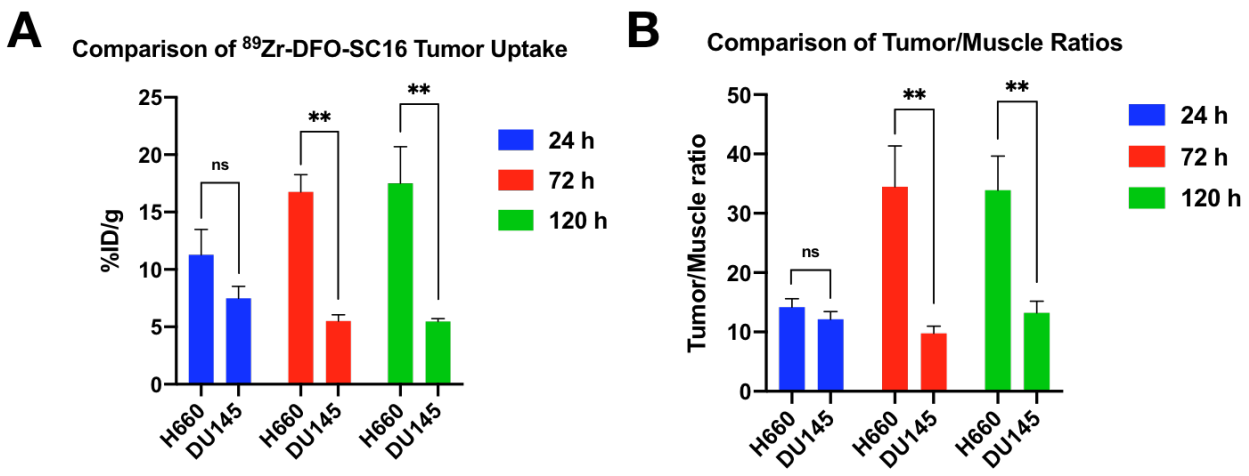

Supplemental Figure 12. DLL3 is specific and selective for DLL3-expressing H660 tumors. **A.** Biodistribution of ^{89}Zr-DFO-SC16 after lateral tail vein injection in H660 xenograft bearing mice and DU145 xenograft bearing mice. The tumoral uptake increases over time in the H660 xenograft. Contrarily, tumor uptake remains relatively constant over the same time frame in the DU145 xenograft. %ID g^{-1}, percentage of injected dose per gram. $^{**}p < 0.01$. **B.** Tumor-to-muscle ratio comparisons over time from the uptake of ^{89}Zr-DFO-S16 in H660 and DU145 xenograft bearing mice. $^{**}p < 0.01$.

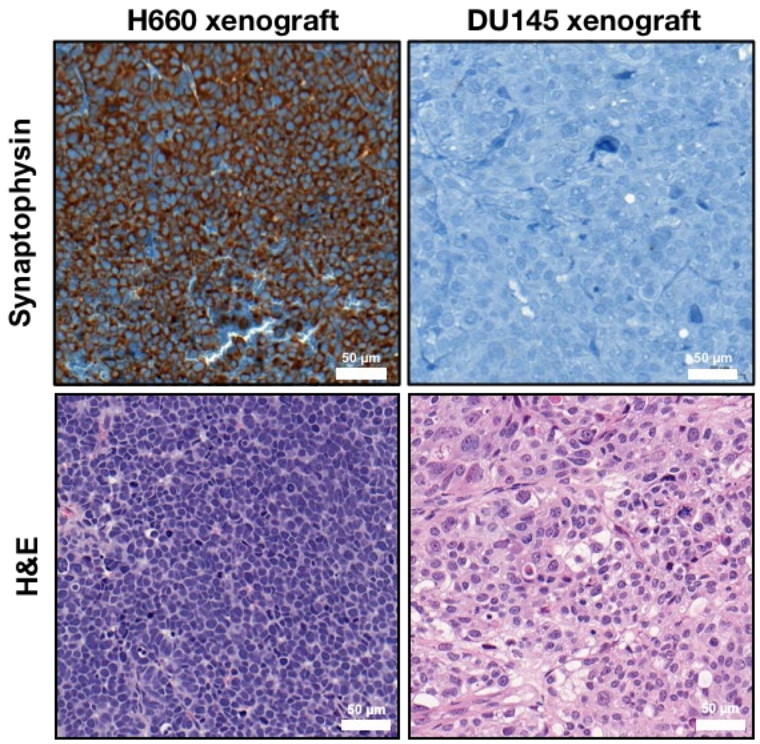

Supplemental Figure 13. Representative immunohistochemistry of H660 and DU145 subcutaneous tumor xenografts for SYP. Additionally, representative H&E images are shown. Scale bars, 50 µm.

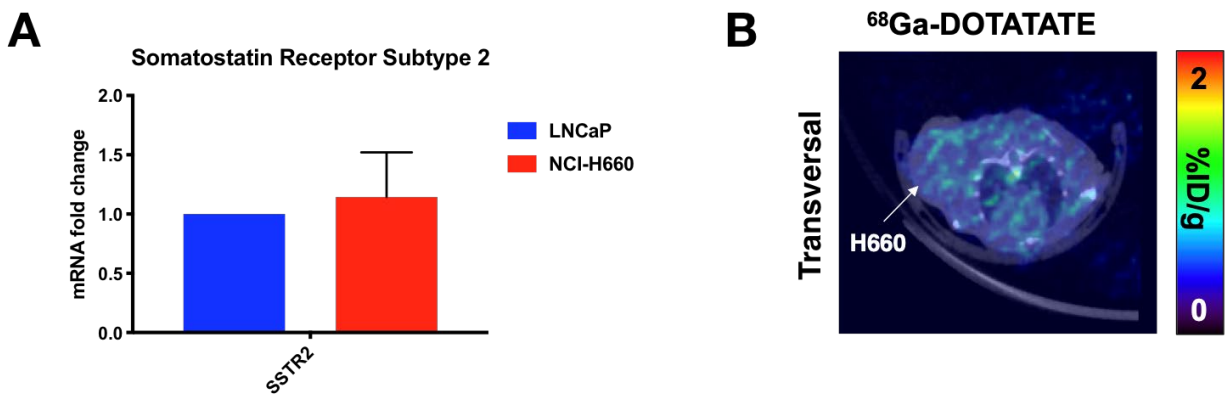

Supplemental Figure 14. ^{68}Ga-DOTATATE cannot image NEPC lesions *in vivo*. A. RT-PCR shows the expression pattern of the SSTR2 gene in H660 as compared to LNCaP cells. No expression of the SSTR2 gene is observed in H660 cells. **B.** PET image of ^{68}Ga-DOTATATE (1h post-injection) in an athymic nude male mouse bearing subcutaneous H660 tumor. Representative transverse planar image is shown.